Chapter 18

Explorational Rock Physics: The Link between Geological Processes and Geophysical Observables

Per Avseth

The field of rock physics represents the link between qualitative geological parameters and quantitative geophysical measurements. Increasingly over the last decade, rock physics has become an integral part of quantitative seismic interpretation and stands out as a key technology in petroleum geophysics. Ultimately, the application of rock physics tools can reduce exploration risk and improve reservoir forecasting in the petroleum industry.

This chapter covers basic rock physics principles and practical recipes that can be applied in the field. The importance and benefit of linking rock physics to geological processes, including depositional and compactional trends, is demonstrated. It is further documented that lithology substitution can be of equal importance to fluid substitution during seismic reservoir prediction. It is essential in exploration and appraisal to be able to extrapolate away from existing wells, taking into account how the depositional environment changes, together with burial depth trends. In this way rock physics can better constrain the geophysical inversion and classification problem in underexplored marginal fields, surrounding satellite areas, or in new frontiers.

Finally, practical examples and case studies are presented to demonstrate a best-practice workflow and associated limitations and pitfalls. Rock physics models are combined with well log and pre-stack seismic data, sedimentological information, inputs from basin modelling and statistical techniques, to predict reservoir geology and fluids from seismic amplitudes.

Per Avseth (✉)
Tullow Oil Norge, Oslo, Norway
NTNU, Trondheim, Norway
e-mail: per.avseth@tullowoil.com

18.1 Quantitative Seismic Interpretation Using Rock Physics

The main goal of conventional, *qualitative* seismic interpretation is to recognise and map geological elements and/or stratigraphic patterns from seismic reflection data. Often hydrocarbon prospects have been defined and drilled entirely on the basis of this qualitative information. Today, however, *quantitative* seismic interpretation techniques have become common oil industry tools for prospect evaluation and reservoir characterisation. The most important of these techniques include post-stack amplitude analysis (bright-spot and dim-spot analysis), offset-dependent amplitude analysis (AVO analysis), acoustic and elastic impedance inversion, and forward seismic modelling. These techniques seek to extract additional information about the subsurface rocks and their pore fluids from the reflection amplitudes and, if used properly, they open up new doors for the seismic interpreter. Seismic amplitudes primarily represent contrasts in elastic properties between individual layers and contain information about lithology, porosity, pore fluid type and saturation, as well as pore pressure – information that cannot be gained from conventional seismic interpretation. Seismic amplitude maps are increasingly important in prospect evaluation and reservoir delineation. As shown in Fig. 18.1, the amplitude patterns often provide a good insight into depositional patterns. Seismic amplitude maps can be very useful in the delineation of subtle traps that are not easily revealed from conventional (i.e. stratigraphic and structural) seismic interpretation.

However, to make sure we understand the meaning of the seismic amplitudes, a quantitative link is needed between the geological parameters and the rock

K. Bjørlykke (ed.), *Petroleum Geoscience: From Sedimentary Environments to Rock Physics*,
DOI 10.1007/978-3-642-34132-8_18,

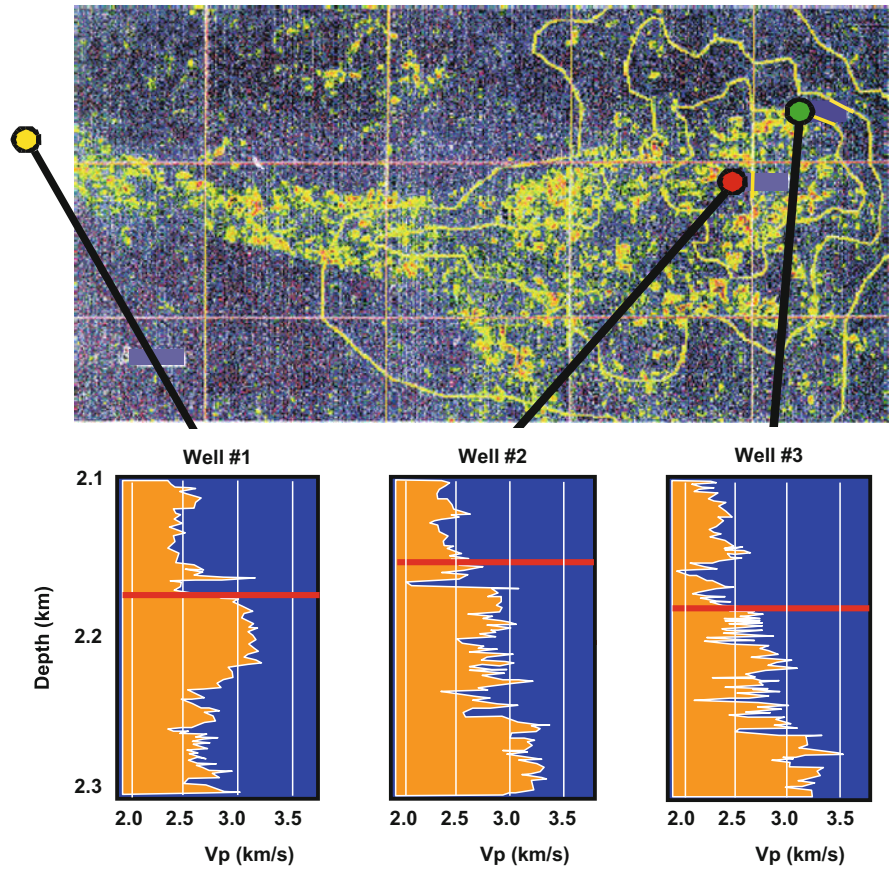

Fig. 18.1 Seismic amplitude map from the Glitne Field, with sonic well log data for three wells penetrating a submarine fan system at different locations. Drastic changes in the seismic velocities and the log patterns are observed as we go from the feeder-channel to the more distal part of the lobe system. (Adapted from Avseth et al. 2005)

physics properties. The seismic reflections are physically explained by contrasts in elastic properties, and rock physics models allow us to link the elastic properties to geological parameters. Hence, the application of rock physics models can guide and improve on the qualitative interpretation (e.g. Mavko et al. 2009, Avseth et al. 2005). Moreover, if we understand the link between geological parameters and rock physics properties, we can avoid certain ambiguities in seismic interpretation, particularly fluid/lithology, sand/shale and porosity/saturation. During fluid substitution, it is very common to assume that the rock type and porosity are constant, neglecting the possibility that lithology can change from the brine zone to the hydrocarbon zone. The link between rock physics and various geological parameters, including cement volume, clay volume and degree of sorting, allow us to perform lithology substitution from rock types observed at a given well location to rock types assumed to be present nearby. Hence, during quantitative seismic interpretation of a reservoir we can do sensitivity analysis not only of fluid types, but also of the reservoir quality.

The way in which geological trends in an area can be used to constrain rock physics models is also investigated. Geological trends can be split into two categories: Depositional and Compactional. If we can predict the expected change in seismic response as a function of depositional environment or burial depth, this will increase our ability to predict hydrocarbons, especially in areas with little or no well log information. Understanding the geological constraints in an area of exploration reduces the range of expected variability in rock properties and hence reduces the uncertainties in seismic reservoir prediction. Figure 18.2 depicts this problem, where the only well

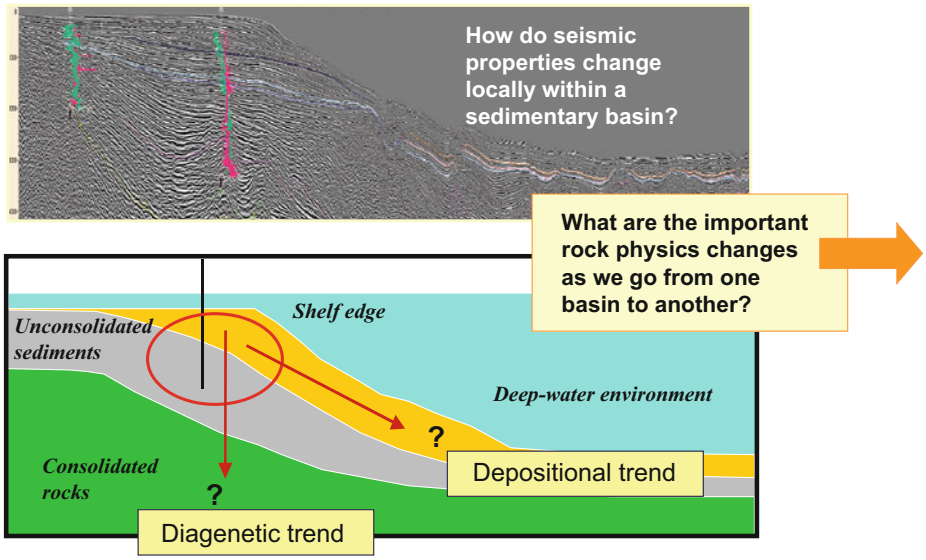

Fig. 18.2 Rock physics properties change with depositional environment and burial depth. These geological trends must be taken into account during hydrocarbon prediction from seismic data

log control we have is in the shallow interval on the shelf edge. Before extending the exploration into more deeply buried zones, or to more distal deepwater environments, it is important to understand the rock physics trends in the area.

18.2 Rock Physics Fundamentals

Rock physics provides a link between geologic reservoir parameters (e.g. porosity, clay content, sorting, lithology, saturation) and seismic properties (e.g. acoustic impedance, the *Vp/Vs* ratio, bulk density and the elastic moduli). Assuming an isotropic, linear elastic material, the stress and strain are related by the famous Hooke's law (Timoshenko and Goodier 1934; Mavko et al. 2009):

$$\sigma_{ij} = \lambda\delta_{ij}\varepsilon_{\alpha\alpha} + 2\mu\varepsilon_{ij} \qquad (18.1)$$

where

ε_{ij} = elements of the strain tensor
σ_{ij} = elements of the stress tensor
$\varepsilon_{\alpha\alpha}$ = volumetric strain (sum over repeated index)
δ_{ij} =0 if i ≠ j and δ_{ij} =1 if i = j.

With the above assumptions, we only need two elastic constants to specify the stress-strain relation completely, i.e. λ and μ, which we often refer to as the Lame's parameters. The first Lame's parameter, λ, can be related to the bulk modulus, K, and the shear modulus, μ, via $\lambda = K - 2\mu/3$. The bulk modulus, K, is defined as the ratio of the hydrostatic stress, σ_0, to the volumetric strain: $\sigma_0 = K\varepsilon_{\alpha\alpha}$. The bulk modulus is the reciprocal of the compressibility, $1/K$, which is used to describe the volumetric compliance of a material. Hence, the bulk modulus expresses a material's resistance to changing its volume V. In a static experiment, the deformations are measured explicitly, as the relative change in volume $\Delta V/V$ caused by a relative change in pressure ΔP, giving the static bulk modulus: $K = \Delta P/(\Delta V/V)$. The shear modulus is defined as the ratio of the shear stress to the shear strain, $\sigma_{ij} = 2\mu\varepsilon_{ij}$, and it expresses the material's resistance to shear deformation. The bulk and shear moduli, which have the same units as stress (force/area, expressed in SI units as Pascal) can be related to seismic compressional (V_P) and shear (V_S) velocities, respectively, according to the following equations:

$$V_P = \sqrt{\frac{K + 4\mu/3}{\rho}} \tag{18.2}$$

$$V_S = \sqrt{\frac{\mu}{\rho}} \tag{18.3}$$

where ρ is the bulk density of the rock. The elastic constants are then referred to as dynamic moduli, which can differ from the static moduli due to difference in strain amplitude. Seismic reflectivity at a rock interface is directly related to the contrast in the dynamic elastic parameters.

Commonly, rock physics analysis is done using crossplots (Fig. 18.3), where observed elastic parameters, either from core, well log or seismic measurements, are plotted versus a given geological parameter. Here, data can be compared with rock physics models to better understand how the geological parameters are controlling the elastic parameters. Rock physics models can also be used to extrapolate beyond the available data range to examine certain "what if" scenarios, such as plausible fluid or lithology variations. In this way, rock physics can be used to forecast seismic response to assumed reservoir and overburden properties and conditions.

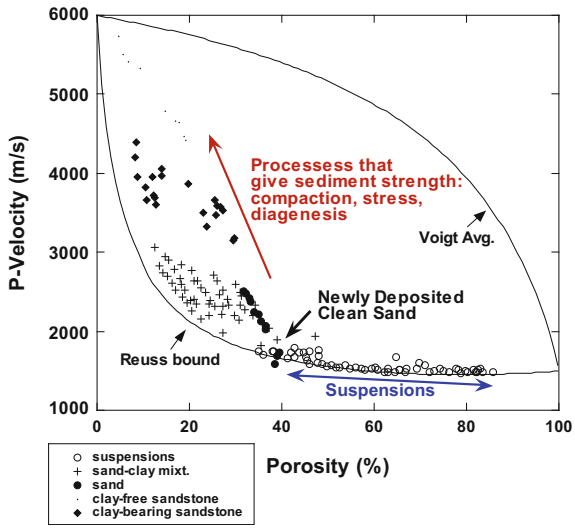

Fig. 18.3 P-wave velocity vs. porosity for a variety of water-saturated sediments, compared with the Voigt-Reuss bounds. Data are from Yin (1992), Han (1986) and Hamilton (1956). (Adapted from Avseth et al. 2005)

Rock physics models also help infer (diagnose) rock texture of sandstones or shales if we know porosity and the elastic-wave velocity. Such diagnostics are based on an assumption that, e.g. if velocity-porosity data fall on a theoretical cemented-rock trend, the rock *is* cemented. This seemingly circular logic helps better understand rock properties beyond elasticity. For example, if rock is cemented, one may expect higher strength than in uncemented rock of the same porosity and mineralogy.

A number of workers (e.g. Vernik and Nur 1992, Dvorkin and Nur 1996, Anselmetti and Eberli 1997) have recognised that the slope of (or impedance-porosity) trends in sandstones is highly variable and depends largely on the geological processes that control porosity. Relatively steep velocity-porosity trends for sandstones are representative of porosity variations controlled by *diagenesis*, i.e. porosity reduction due to pressure solution, compaction and cementation. Hence, we often see steep velocity-porosity trends when examining data spanning a great range of depths or ages. The classical empirical trends of Wyllie et al. (1956), Raymer et al. (1980), Han (1986) and Raiga-Clemenceau et al. (1988), all show versions of the steep, diagenetically-controlled velocity-porosity trend. On the other hand, porosity change resulting from variations in sorting and clay content tend to yield much flatter velocity-porosity trends, meaning that porosity controlled by *sedimentation* is generally expected to yield flatter trends, which we sometimes refer to as *depositional trends*. Data sets from narrow depth ranges, or individual reservoirs often (though not always) show this behaviour.

There is a wide range of different models that can be used in rock physics analysis (Mavko et al. 2009, Dræge et al. 2006). Every model has certain advantages and limitations. We follow Box and Draper (1987) in believing that: "All models are wrong, but some are useful". There are in general three different classes of models: theoretical, empirical, and heuristic. In this chapter we show applications of a hybrid approach where we combine theoretical contact theory (granular media) or pore-shape constrained models with heuristic bounds to predict sedimentary microstructure and geologic trends from elastic properties.

In particular, we have found that diagenetic trends, which connect newly-deposited sediment on the Reuss elastic bound with the mineral point at zero porosity,

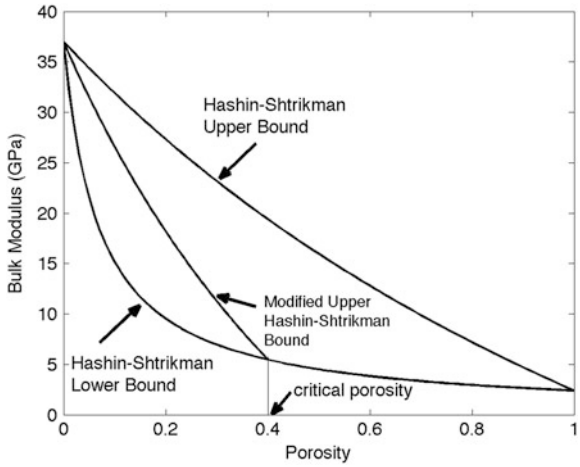

Fig. 18.4 Hashin-Shtrikman and modified Hashin-Shtrikman bounds for bulk modulus in a quartz-water system (Adapted from Avseth et al. 2010)

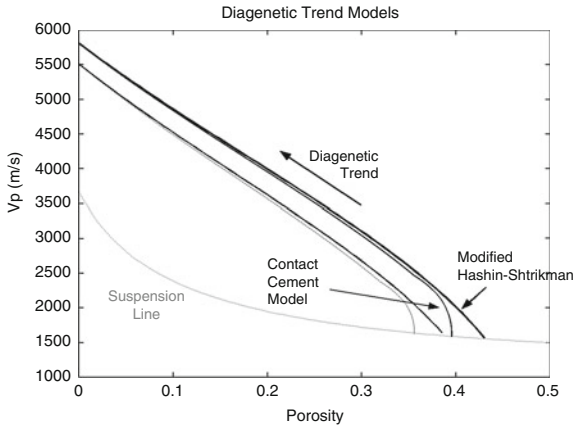

Fig. 18.5 Appending Dvorkin-Nur's contact cement model at the high porosity end of the modified Hashin-Shtrikman bound improves the agreement with sands (Adapted from Avseth et al. 2010)

can often be described accurately using the *upper Hashin-Shtrikman bound*, see Fig. 18.4. In fact, we sometimes refer to it as a *modified upper Hashin-Shtrikman bound* because we use it to describe a mixture of the newly deposited sediment at critical porosity with additional mineral, instead of describing a mixture of mineral and pore fluid. A slight improvement over the modified upper Hashin-Shtrikman bound as a diagenetic trend for sands can be obtained by steepening the high porosity end. An effective way to do this is to use Dvorkin's model (Dvorkin and Nur 1996) for cementing of grain contacts. The contact cement model captures the rapid increase in elastic stiffness of a sand, without much change in porosity as the first bits of cement are added (Fig. 18.5).

The depositional or sorting trends can be described with a series of *modified Hashin-Shtrikman lower bounds* (Fig. 18.6). By combining the contact cement model with such sorting trends, we can create lines of constant depth, but variable texture, sorting and/or clay content. For more details and equations behind these models, see Avseth et al. (2005). Below, we demonstrate how we can use these models to quantify the rock texture of sandstones based on North Sea well data.

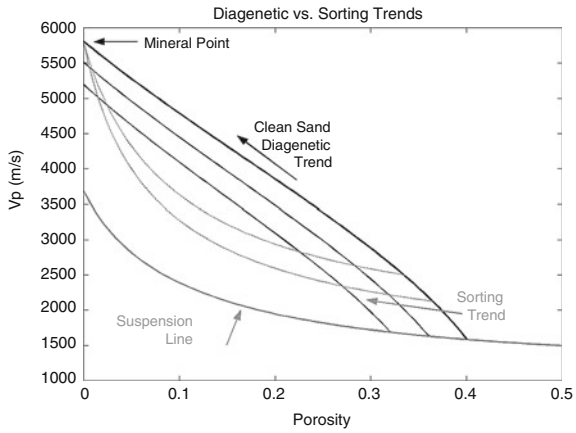

Fig. 18.6 Generalised clastic model. Sediments are deposited along the suspension line. Clean, well sorted sands will have initial (critical) porosity of ~0.4. Poorly sorted sediments will have a smaller critical porosity. Burial, compaction and diagenesis move data off the suspension line. Sediments of constant shaliness or sorting and variable age (or degree of diagenesis) fall along the (*black*) cementing trends. Sediments of constant age, but variable shaliness or sorting will fall long the (*grey*) sorting trends. (Adapted from Avseth et al. 2010)

In order to interpret the observed seismic contrast, we also need to know the rock properties of shales. These require more complex rock physics models to capture crack-like pore shapes, intrinsic microporosity, transverse isotropy and diagenetic mineral transitions. So-called inclusion-based models where solids are filled with pores of different shapes and concentrations (e.g. Differential Effective Medium model, Self-Consistent Approach; see Mavko et al. 2009) have proven useful for shales and low-porosity sandstones

where pores are poorly connected (e.g. Hornby et al. 1994, Johansen et al. 2002, Avseth et al. 2014), and where contact theory and granular-based models presented above are not representative or valid. For shales and heterogeneous sandstones it may be important to take into account the anisotropy effect on seismic velocities (e.g. Golikov et al. 2013). The sedimentological layering of interbedded sands and shales, and the internal texture of shale, will yield transverse isotropy, where seismic waves propagating in the vertical direction will travel at a slower velocity than seismic waves propagating in the horizontal direction. In an isotropic medium we are only dealing with two independent elastic constants as given in the isotropic version of Hooke's law (Eq. 18.1). Assuming an anisotropic, linear, elastic solid, Hooke's law can be expressed in compact form as follows:

$$\sigma_{ij} = c_{ijkl}\varepsilon_{kl} \tag{18.4}$$

where the stiffness tensor is a fourth rank tensor and has 81 components. However, not all the components are independent. Symmetry of stresses and strains implies that the number of independent constants reduces to 36. The existence of a unique strain energy potential further reduces it to 21. And for a transverse isotropic medium, where the vertical axis lies along the axis of symmetry, the number of independent constants are reduced to 5. With simplified Voigt annotation (see Mavko et al. 2009) the elastic stiffness tensor can then be expressed as:

$$\mathbf{C} = \begin{vmatrix} C_{11} & (C_{11}-2C_{66}) & C_{13} & 0 & 0 & 0 \\ (C_{11}-2C_{66}) & C_{11} & C_{13} & 0 & 0 & 0 \\ C_{13} & C_{13} & C_{33} & 0 & 0 & 0 \\ 0 & 0 & 0 & C_{44} & 0 & 0 \\ 0 & 0 & 0 & 0 & C_{44} & 0 \\ 0 & 0 & 0 & 0 & 0 & C_{66} \end{vmatrix},$$

$$\text{where } C_{66} = \frac{1}{2}(C_{11} - C_{12}) \tag{18.5}$$

This 6 × 6 matrix is symmetric and the five independent components are annotated C_{11}, C_{13}, C_{33}, C_{44}, and C_{66}. These are not easily related to geological parameters as the shear and bulk moduli, but Thomsen (1986), assuming weak anisotropy, expressed three anisotropic parameters, ε, γ and δ as a function of the five elastic components, where:

$$\varepsilon = \frac{C_{11} - C_{33}}{2C_{33}} \tag{18.6}$$

$$\gamma = \frac{C_{66} - C_{44}}{2C_{44}} \tag{18.7}$$

$$\delta = \frac{(C_{13} + C_{44})^2 - (C_{33} - C_{44})^2}{2C_{33}(C_{33} - C_{44})} \tag{18.8}$$

The constant ε can be seen to describe the fractional difference of the P-wave velocities in the vertical and horizontal directions:

$$\varepsilon = \frac{V_P(90^\circ) - V_P(0^\circ)}{V_P(0^\circ)} \tag{18.9}$$

and is usually referred to as "P-wave anisotropy".

In the same manner, the constant γ can be seen to describe the fractional difference of SH-wave velocities (horizontally polarised shear wave velocity) between vertical and horizontal directions, which is equivalent to the difference between the vertical and horizontal polarisations of the horizontally propagating S-waves:

$$\gamma = \frac{V_{SH}(90^\circ) - V_{SV}(90^\circ)}{V_{SV}(90^\circ)} = \frac{V_{SH}(90^\circ) - V_{SH}(0^\circ)}{V_{SH}(0^\circ)} \tag{18.10}$$

The physical meaning of δ is not as clear as ε and γ, but δ is the most important parameter for normal move out velocity and reflection amplitude.

Later in this chapter, we will show how we can utilise rock physics models to calibrate seismic amplitude data, and to help us predict lithology and fluids prior to drilling, and we will also demonstrate how we can take into account shale anisotropy in our analysis. Rock physics theory and models for fluid effects are included in a separate section later in this chapter (Sect. 18.6).

18.3 Rock Physics Models for Microstructure Interpretation

Rock physics models can either be used to interpret observed sonic and seismic velocities in terms of

reservoir parameters, or they can be used to extrapolate beyond an observed range to predict certain "what if" scenarios in terms of fluid or lithology substitution. Rock physics models can also be used to estimate expected seismic properties from observed reservoir properties. Pore fluid and stress sensitivity in reservoir sandstones are highly affected by reservoir heterogeneity and sandstone microstructure, and it is therefore important to include these geological factors in the rock physics analysis.

Using the diagnostic models described in Sect. 18.2, we can infer the microstructure from velocity-porosity data (e.g. Dvorkin and Nur 1996, Avseth et al. 2000, 2010). With good local validation of the models, we can even quantify the degree of sorting and cement volume from these diagnostic crossplots.

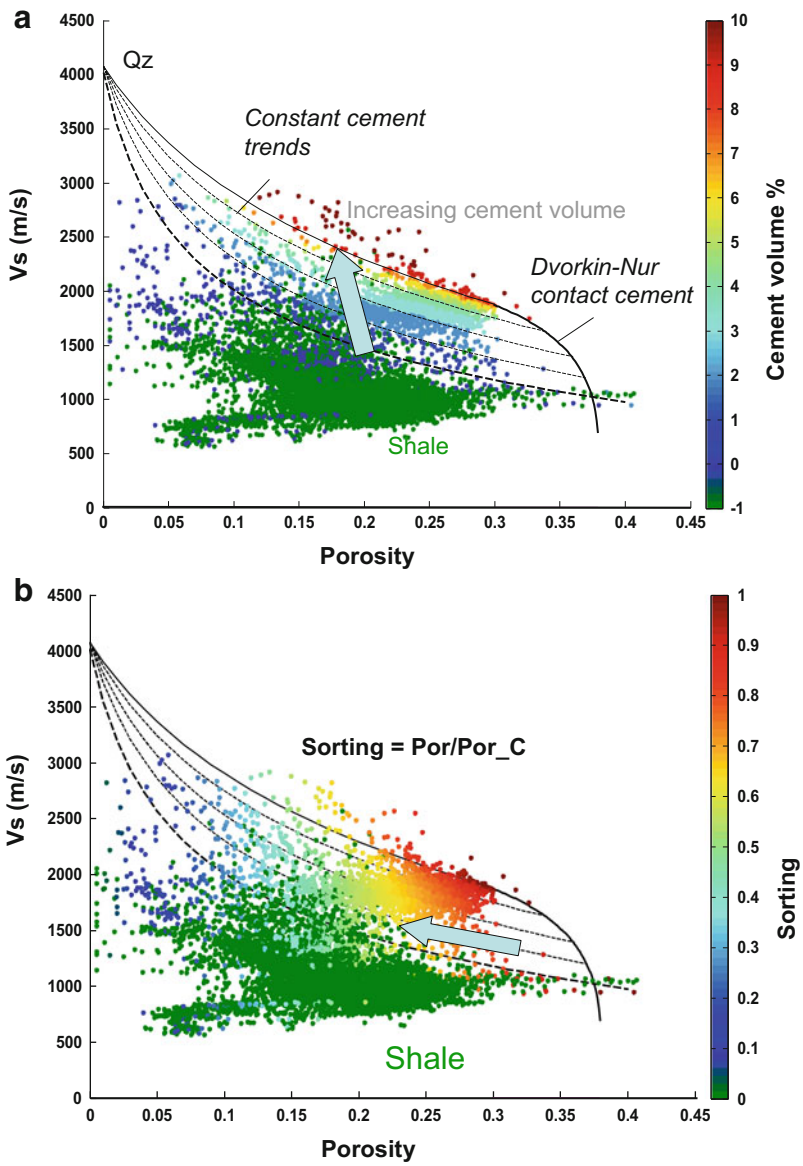

Fig. 18.7 Shear wave velocity log data versus total porosity and superimposed diagnostic rock physics models. Using the models we can quantify the cement volume (**a**) and degree of sorting (**b**) (*Green* data points are shale data with high GR values, and for practical reasons are given the value –1 in cement volume and 0 in sorting). (Taken from Avseth et al. 2009)

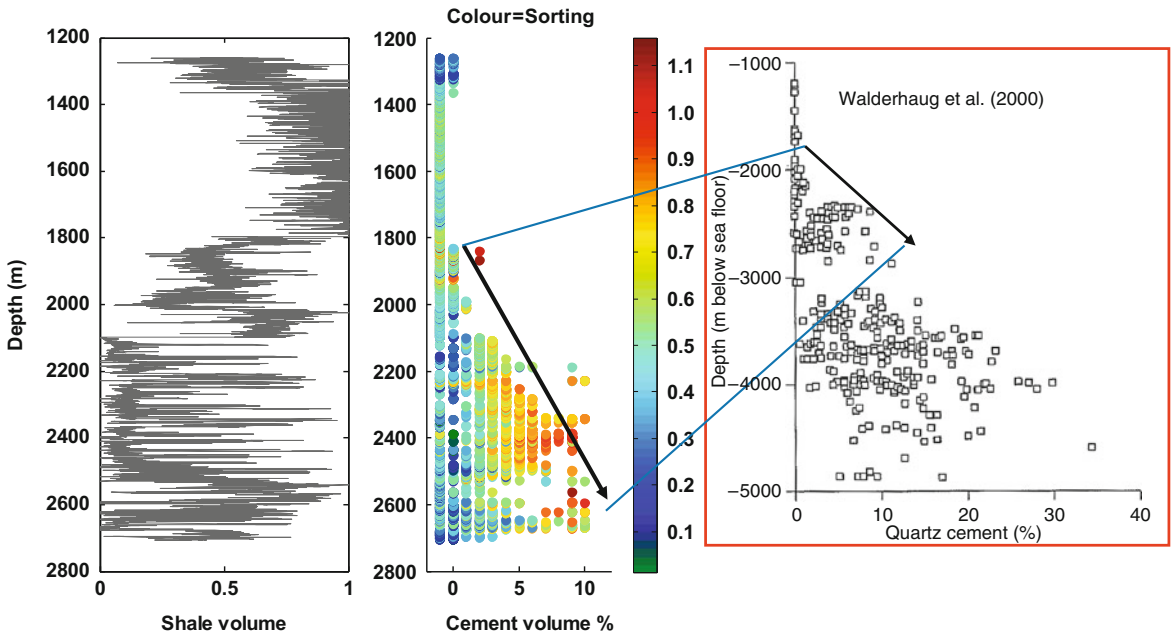

Fig. 18.8 Estimated cement volume and sorting versus depth for a North Sea well. Note the onset of cement at around 2,000 m depth (corresponding to c.70°C) and the increasing cement volume with depth (*second column*). This is in agreement with observations made by Walderhaug et al. (2000). Sorting, however, shows a more erratic pattern with no depth trend (*colour in second column*; see also Avseth et al. 2009)

Figure 18.7 shows an example from Avseth et al. (2009). Here, the rock physics diagnostics is done in the *Vs* versus porosity domain, in order to avoid significant pore fluid effects. The cement volume is estimated by interpolating between the constant cement volume trends. For a given constant cement trend, sorting is defined to vary between 1 and 0. Sorting equals 1 for data points that fall right on the contact cement model. Deteriorating sorting implies increasing volume of pore-filling (non-cementing) material which will cause lower porosities. The data points will then plot further away from the contact cement model, towards zero porosity. At the zero porosity end member, sorting is defined to be zero. It is important to note that this definition of sorting is not the same as the qualitative sorting parameter defined in the field of sedimentology, but they will be highly correlated, with values approaching 0 when sands are poorly sorted and values approaching 1 when sands are well sorted.

Having estimated cement volume and sorting, we can plot these as logs and compare with other petrophysical logs. Figure 18.8 shows the resulting estimation of cement volume and sorting. The middle subplot shows cement volume as magnitude, with sorting as superimposed colour. For the relatively clean Heimdal sandstones starting at around 2 km depth, we observe a clear depth trend in the cement volume. This matches observations made by Walderhaug et al. (2000) (Fig. 18.8, right subplot). The sorting shows a more erratic pattern, lacking any consistent depth trend, as we would expect since sorting is associated with depositional trends.

It is essential to verify with thin section observations the presence of initial cementation predicted from the rock physics relations. Figure 18.9 shows a thin-section from the relatively clean Heimdal sands, but at first glance the sandstone looks unconsolidated with grains loosely arranged and moderately well sorted. A closer investigation, however, reveals the presence of initial quartz overgrowth covering original grain surfaces, indicated by dust rims (see arrows, Fig. 18.9). This observation confirms what we see in the rock physics crossplots of the well log data. It is interesting that the well log data with 10s of cm resolution reflect what we observe at the micro-scale. A comparison between cement volume estimated from rock physics models and the cement volume from the thin-section point count analysis (only available in the

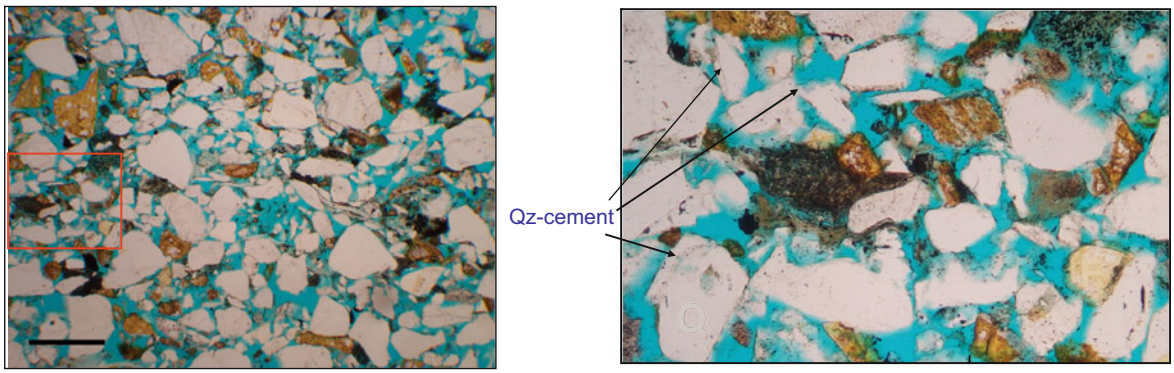

Fig. 18.9 Thin sections from Heimdal Formation sands. The *left image* shows a loosely packed, poorly consolidated sand. Analysis of a zoomed-in image (*right*) confirms the presence of quartz overgrowths and contact cement. On detrital quartz grains we observe dust rims representing the original grain surfaces that have been covered by quartz cement (*arrows*). Feldspar overgrowth and calcite cement also occur, though quartz cement is dominating. (From Avseth et al. 2009)

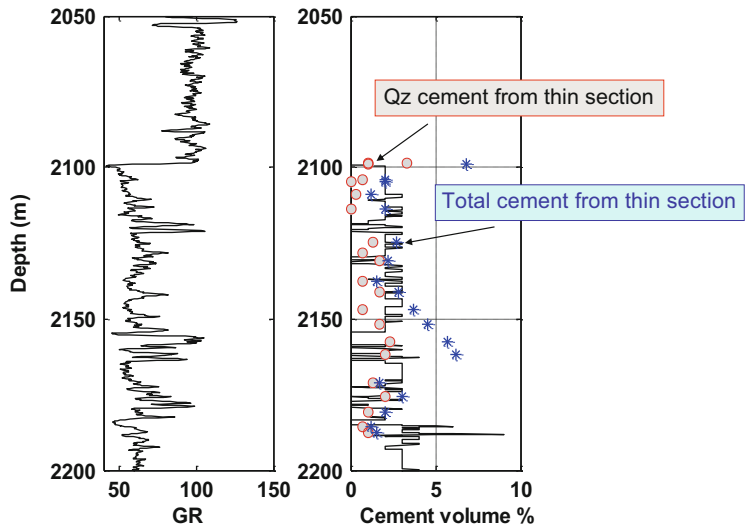

Fig. 18.10 The estimated cement volume based on rock physics models (*black line* in *right-hand subplot*) compared with point-count cement volume in the *upper* 100 m of the Heimdal reservoir sands in the well analysed in Figs. 18.7 and 18.8. The estimated cement volume is slightly larger than the point-counted quartz cement, but for most of the depth-range it matches nicely with the point-counted total cement volume. (From Avseth et al. 2009)

upper part of the Heimdal sands in the well analysed in Figs. 18.7 and 18.8) is shown in Fig. 18.10. The volume of quartz cement from the thin-section analysis is somewhat lower than the volume estimated from the rock physics models. However, if we compare the rock physics estimates with the total cement volume, the match is very good. While most of the cement in the Heimdal Fm is quartz in this well, other types are also present, like feldspar overgrowths and carbonate cement (see also Lehocki and Avseth 2010).

18.4 Rock Physics and Depositional Trends

There exist several rock physics models for depositional trends in siliciclastic environments (e.g. Marion 1990, Dvorkin and Gutierrez 2002, Xu and White 1995). Marion (1990) introduced a topological model for sand-shale mixtures to predict the interdependence between velocity, porosity and clay content. When clay content is less than the sand porosity, clay

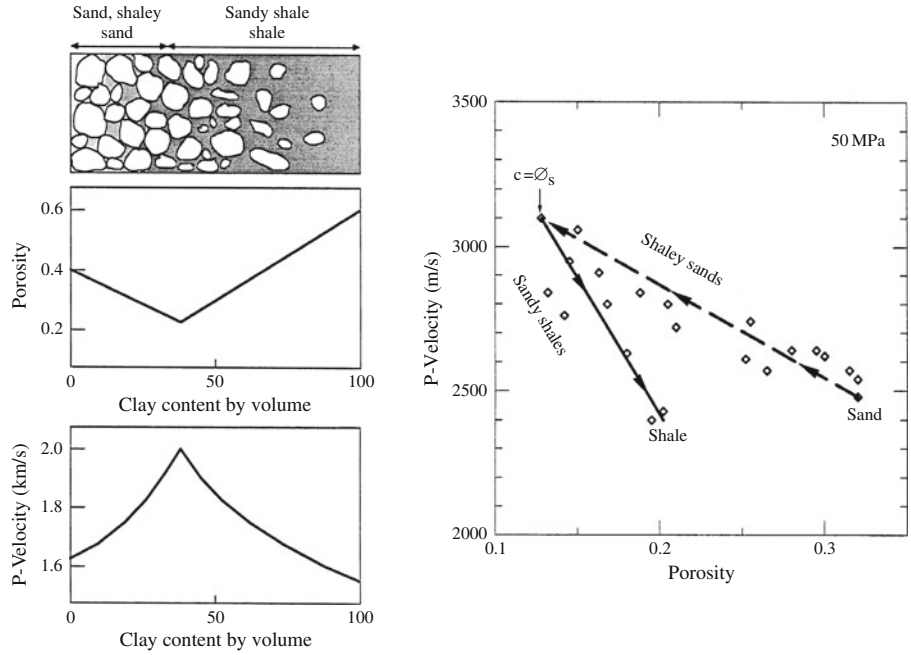

Fig. 18.11 *Left*: The Yin-Marion topological model of porosity and P-wave velocity versus clay content for shaly sands and sandy shales (from Marion 1990). *Right*: Laboratory experiments (Yin 1992) showing P-wave velocity versus porosity for unconsolidated sands and shales at constant effective pressure of 50 MPa. A clear V-shape trend is observed with increasing clay content, where velocity reaches a maximum and porosity a minimum when the clay content equals the sand porosity

particles are assumed to be located within the pore space of the load-bearing sand. The clay will stiffen the pore-filling material, without affecting the frame properties of the sand. Therefore, increasing clay content will increase the stiffness and velocity of the sand-shale mixture as the elastic moduli of the pore-filling material (fluid and clay) increase. Once the clay content exceeds the sand porosity, the addition of more clay will cause the sand grains to become separated, as we go from grain-supported to clay-supported sediments (i.e. shales).

Marion assumed that, similar to fluids, the pore-filling clay would not significantly affect the shear modulus of the rock. This assumption was supported by laboratory measurements on unconsolidated sand-shale mixtures (Yin 1992). The impact on the velocity-porosity relationship of increasing clay content in a sand/shale mixture is depicted in Fig. 18.11. From the measured data we can see that when clay content increases, porosity decreases and velocity increases up to a given point called the *critical clay content*. This point represents the transition from shaly sands to sandy shales. After this point, porosity increases with increasing clay content, and velocity decreases. It also has to be mentioned that clay particles can be deposited as lamina between sand grains or intervals of sands, and these will yield a completely different elastic response than pore-filling clays (e.g. Sams and Andrea 2001).

Until recently, shales have often been regarded by geophysicists as a single type of lithology, with little attention given during seismic data analysis to the wide variation in their mineralogy, texture and porosity. This is partly because the rock properties of clay minerals are difficult to measure in the laboratory, but also because the acquisition of detailed log data and core samples in shale sequences has been given little priority in the oil industry. Geologists, however, have documented the complexity of shales and there is a vast amount of published literature on the geochemistry and sedimentology of shales (e.g. Bjørlykke 1998, MacQuaker et al. 2007, Peltonen et al. 2008). With increased focus on cross-disciplinary integration, geophysicists are starting to incorporate this geological knowledge into the modelling and analysis of geophysical data (e.g. Dræge et al. 2006, Brevik et al.

2007, Mondol et al. 2007, Marcussen et al. 2009). As with sands, we can distinguish between depositional and diagenetic trends in shales. Depositional trends will affect clay mineralogy, but more particularly, the silt content will have great impact on the seismic properties. Avseth et al. (2005) used simple isotropic lower Reuss bound to model vertical velocities of silty shales. More rigorous anisotropic modelling of shales has been performed by Hornby et al. (1994), Ruud et al. (2003), Johansen et al. (2002) and Dræge et al. (2006), among others.

One of the fundamental aspects of this chapter is to establish a link between rock physics and sedimentology. More specifically, we want to relate lithofacies to rock physics properties. This will improve our ability to use seismic amplitude information to interpret depositional systems, as facies have a major control on depositional geometries and porosity distributions. Furthermore, facies occur in predictable patterns in terms of their lateral and vertical distribution, and can also be linked to sedimentary processes. Hence, facies represent an important parameter in seismic exploration and reservoir characterisation.

Avseth et al. (2001a) defined *seismic lithofacies* as a seismic-scale sedimentary unit which is characterised by its lithology (sand, silt and clay), bedding configuration (massive, interbedded or chaotic), petrography (grain size, clay location and cementation) and seismic properties (P-wave velocity, S-wave velocity, and density). Using the concept that seismic lithofacies represent seismic-scale sedimentary units, we can improve our lateral facies prediction, as we can link facies observed in vertical well logs to seismic attribute maps in accordance with Walther's law of facies (e.g. Middleton 1973).

In the Glitne turbidite system depicted in Fig. 18.1, Avseth et al. (2001a) identified various seismic lithofacies in turbidite systems (I = conglomerates/gravels, II = massive sandstones, III = interbedded sands-shales, IV = silty shales, V = shales), and these represent a more or less gradual transition from clean sandstone to pure shale. Three subfacies of Facies II are defined based on seismically important petrographic variations within the thick-bedded sand facies. These subfacies were determined from core, thin-section and SEM analyses, in combination with rock physics diagnostics, and include cemented clean

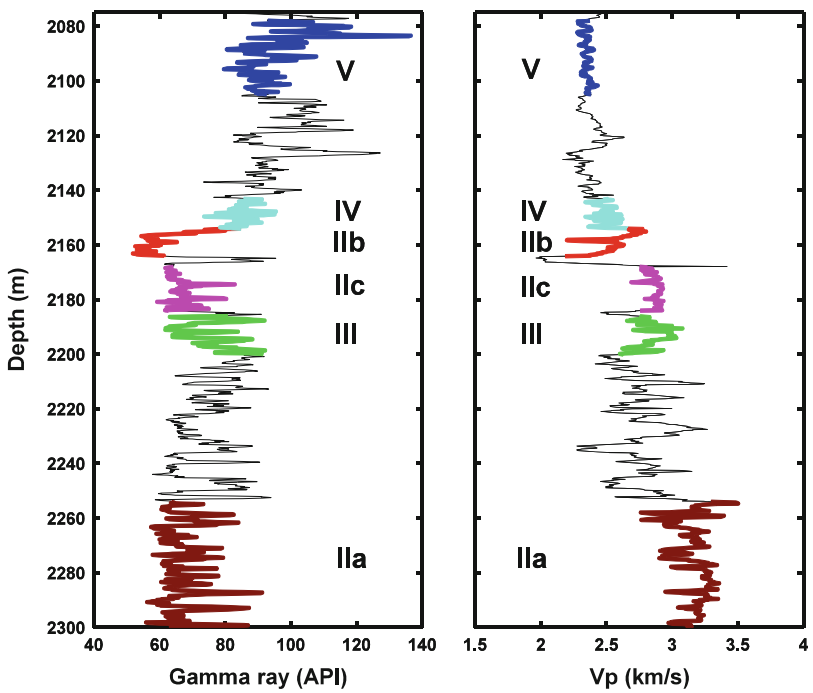

Fig. 18.12 Identifying seismic lithofacies from well log data; example from Palaeocene interval in the Glitne Field, North Sea. (From Avseth et al. 2001a)

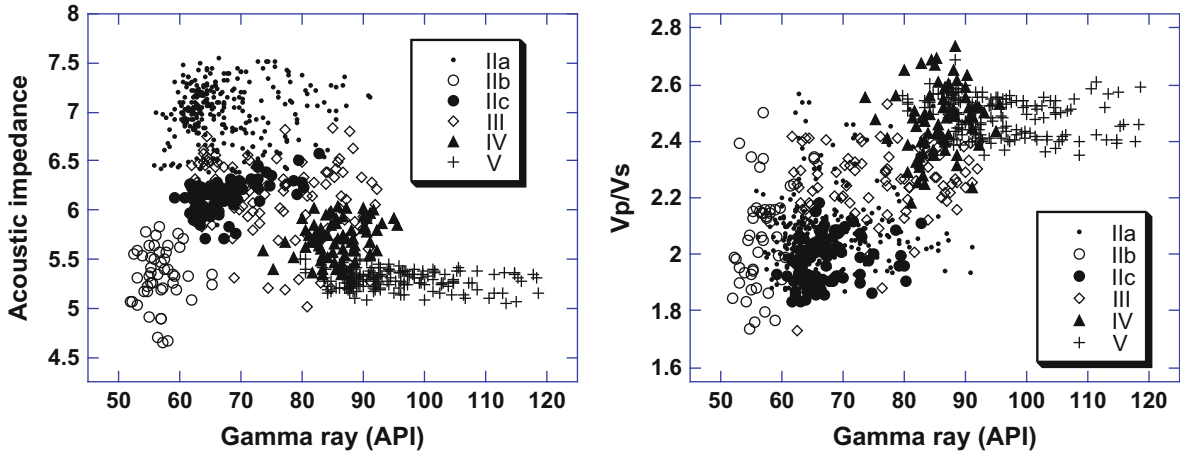

Fig. 18.13 Acoustic impedance (in km/s*g/cm^3) and *Vp/Vs* ratio versus gamma ray for different seismic lithofacies in the Glitne turbiditic field depicted in Fig. 18.1. Note the overturned V-shape in the *left hand subplot*, where clean sands and shales have similar acoustic impedance values, whereas shaly/interbedded sands have relatively high impedance values. In the *Vp/Vs* versus gamma ray plot, we observe a more linear trend as we go from clean sands to shaly facies. (From Avseth et al. 2001a)

sands (Facies IIa), uncemented or friable clean sands (Facies IIb) and plane-laminated sands (Facies IIc). Our seismic lithofacies can be linked to depositional sub-environments and sedimentary processes within a deepwater clastic system (e.g. Walker 1978, Reading and Richards 1994).

Avseth et al. (2001a) selected a type-well for identification of seismic lithofacies from well log data (Fig. 18.12). Primarily, the gamma ray log was used to determine the different facies, as it is a good clay indicator in the quartz-rich sediments of the North Sea. Density and sonic logs were also used to ensure that each facies occurs as significant clusters in terms of rock physics properties. Rock physics analysis can furthermore be used diagnostically to determine lithofacies when direct core and thin-section data are not available. This was essential in order to confirm the presence of cement in Facies IIa. The cementation in Facies IIa is volumetrically not very significant, but in terms of elastic properties it has an important impact. The seismic velocities and impedances are relatively high because of the stiffening effect of initial cementation.

Figure 18.13 shows the different seismic lithofacies plotted as acoustic impedance versus gamma ray (left), and *Vp/Vs* versus gamma ray (right). For acoustic impedance, we observe an overturned V-shape, and an ambiguity exists between Facies IIb and IV/V. Cemented sands (IIa) and laminated sands (IIc), as well as interbedded sand-shales have relatively high impedances. The sand-shale ambiguity is not observed in the *Vp/Vs* versus gamma ray plot. Here we see a more linear trend where *Vp/Vs* increases with increasing gamma ray values (i.e. clay content) as we go from clean sands (Facies IIa and IIb) to shales (Facies IV and V). The overturned V-shape we observe in acoustic impedance can be explained physically: for grain-supported sediments, increasing clay content tends to reduce porosity (i.e. increase density) and therefore stiffen the rock. However, for clay-supported sediments, porosity will increase with increasing clay content due to the intrinsic porosity of clay, and the rock framework will weaken. Hence, velocity will reach a peak when clay content is approximately 40%, cf. the Yin-Marion model shown in Fig. 18.11. Higher *Vp/Vs* ratios are expected in shales than sands, since the shear strength in shales tends to be relatively low compared to sands, due to the platy shapes of clay particles.

18.5 Rock Physics and Compactional Trends

Rock physics depth trends are important in seismic exploration and borehole drilling for several reasons. Commonly, overpressured zones can be detected from

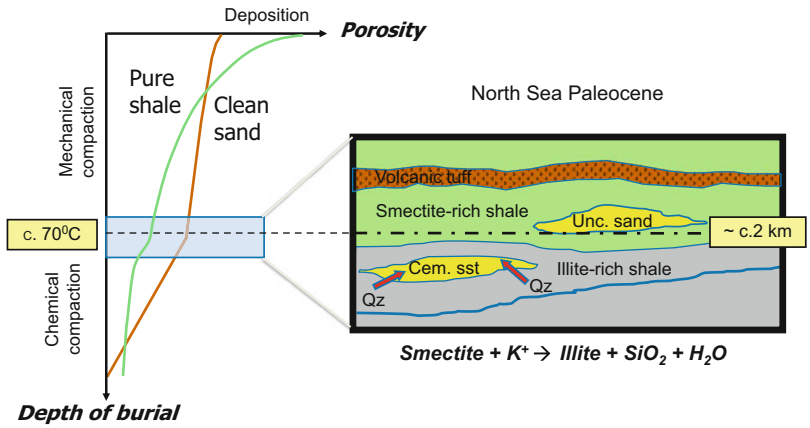

Fig. 18.14 Schematic illustration of sand and shale compaction. At c.70°C it is common to observe a change from mechanical compaction to predominantly chemical compaction in siliciclastic systems. In deep-marine depositional systems, smectite-rich shales will experience illitisation and release of bound water, causing both a porosity reduction and mineralogy change with depth. For quartz-rich sands, initial cementation tends to start at the same depth level. One possible external source of cement is in fact derived from the smectite to illite transition in embedding shales. (From Avseth et al. 2008)

seismic velocity data, indicated by negative velocity anomalies. Knowing that effective pressure and pore pressure increase linearly with depth, rock physics depth trends can be used to quantify overpressure. It is extremely important to locate such zones since they can cause hazardous blowouts during drilling. The depth trends for sands and shales can also be used to study the expected seismic signatures of sand/shale interfaces as a function of depth.

In this section, we use existing empirical porosity/depth trends for sands and shales as input to rock physics models of *Vp*, *Vs* and density. We can for example use Hertz-Mindlin theory (Mindlin 1949; Chap. 19) to calculate the velocity/depth trends for unconsolidated sands and shales, whereas Dvorkin-Nur's contact-cement model (Dvorkin and Nur 1996) can be used for cemented sands. The depth trends allow us to discriminate between pore fluids and lithologies at different depths.

Figure 18.14 shows a schematic representation of shale and sand compaction curves, and a sequence of interbedded turbidite sands and marine shales, typical for the North Sea deep-marine environment of Tertiary age. The depositional porosity in shales is normally much higher (60–80%) than in sands (c. 40%), but we expect a shallow crossover with depth due to the mechanical collapse of the shales. The platy clay fabric in the shales is more prone to compaction than the assemblage of spherically shaped grains in sands, hence the more rapid mechanical porosity reduction in shales than sands. During burial to ~2 km depth, both sands and shales are exposed mainly to mechanical compaction. The marine shales in the North Sea Tertiary are very rich in smectite, which gives them very low permeability. In thick smectite-rich shale masses, it is therefore normal to observe undercompaction and associated overpressure even at burial depths of just several hundred metres. At about 70°C, however, chemical alteration of smectite will commence and we expect a mineral transformation to illite. This is a typical mineral transformation seen in marine shales all over the world (Bjørlykke 1998). Bound water in the smectite layers is released when the temperature reaches this critical temperature, resulting in a porosity decrease. Moreover, the presence of potassium cations (for instance in feldspar or mica) causes quartz to be produced as well. This quartz can precipitate as microcrystalline quartz within the shale matrix (Thyberg et al. 2009), or if connectivity allows, the quartz may precipitate as cement in adjacent sandstones (Peltonen et al. 2008).

Even though there can be a link between the quartz cementation of sandstones and illitisation of smectite-rich shales, it is important to note that the source of quartz cement in sandstones can result from a variety of geological processes (Worden and Morad 2000). Figure 18.14 also includes a volcanic tuff layer that is typically encountered in the Tertiary of the North

Sea (i.e. within the Balder Formation). Smectite is often generated from the alteration of volcanic tuff, but tuff also includes amorphous silica that can precipitate as quartz cement even at temperatures below 70°C. Amorphous silica is thus able to dissolve at lower temperatures than crystalline quartz.

There are also potential internal sources of quartz cement in the sandstones, either from authigenic or detrital clays in the sandstone matrix, or from the quartz grains themselves. Moreover, it has been confirmed that clay minerals can both inhibit the precipitation, and catalyse the dissolution, of quartz in sandstones. The presence of oil has also been shown to inhibit quartz cementation in oil-wetting sandstones (e.g. Giles et al. 2000). There is considerable debate among geologists over whether effective pressure at quartz grain contacts in sandstones can cause quartz dissolution and re-precipitation around the grain contacts. More likely, time and temperature control the quartz cementation (e.g. Bjørlykke and Egeberg 1993).

Regardless of the complexity of the clay and quartz diagenesis, there is empirical evidence that both the smectite to illite transformation in shales and the quartz cementation of sandstones are geochemical processes that tend to initiate concurrently at around 70–80°C. In the North Sea, this corresponds to a burial depth of about 2 km which is around the target depth of the prolific Palaeocene and Eocene reservoir sands that represent major prospects for the oil industry. Geophysicists should be focused on these geological factors during seismic data analysis of reservoir sands, because dramatic changes in the seismic signatures may reflect not pore fluid changes, but diagenetic alterations in the cap-rock shales and/or reservoir sandstones.

Figure 18.15 shows well log data from a North Sea well that penetrates siliciclastic sediments and rocks of Tertiary age, superimposed with rock physics depth trends for shales and sandstones. We observe a nice match between the calculated velocity depth trends for different lithologies and the well log data. The sandstone rock physics depth trends are modelled by combining Hertz-Mindlin contact theory (see Chap. 19) for unconsolidated sands with the Dvorkin-Nur contact cement model for cemented sandstones (Dvorkin and Nur 1996, Avseth et al. 2003, 2005, 2008). The input porosity/depth trends are calibrated with local compaction trends according to empirical relations (e.g. Mondol et al. 2007, Ramm and Bjørlykke 1994). The light blue model trend curves in Fig. 18.15 show how

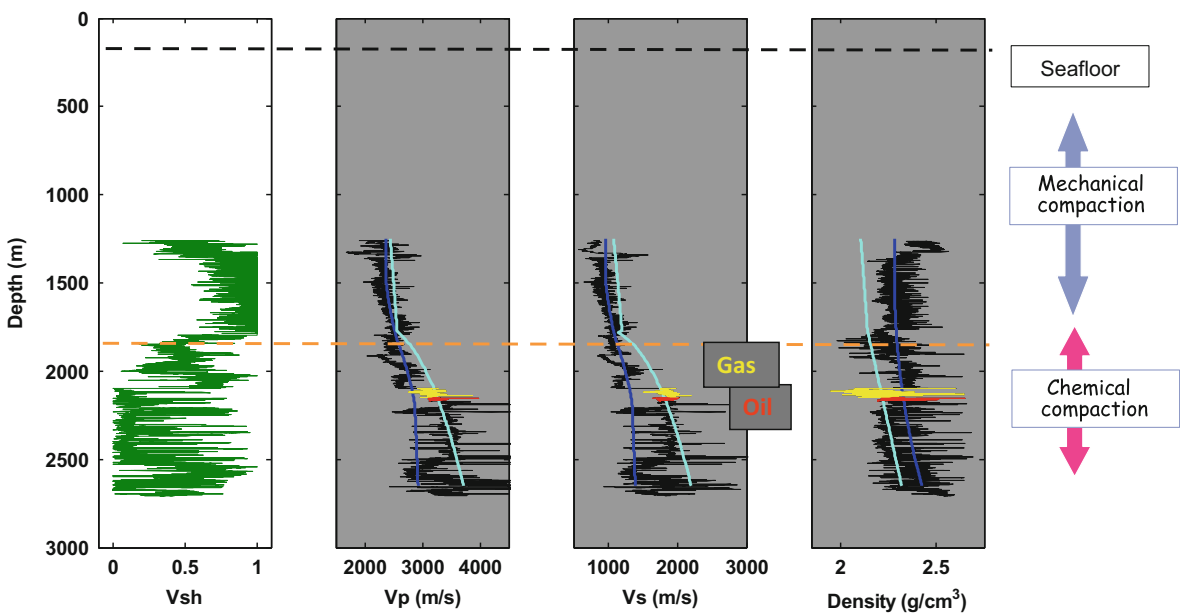

Fig. 18.15 Rock physics depth trends for shales (*dark blue*) and sandstones (*cyan*) juxtaposed on North Sea well log data penetrating a Tertiary sequence of siliciclastic sediments and rocks (same well data as in Fig. 18.8). A gas zone is indicated in *yellow* (2,099–2,151 m), and an oil zone in *red* (2,151–2,168 m). The remaining interval of the Heimdal Formation is brine-filled. The Heimdal Formation is embedded in the Lista Formation shale. (Adapted from Avseth et al. 2008)

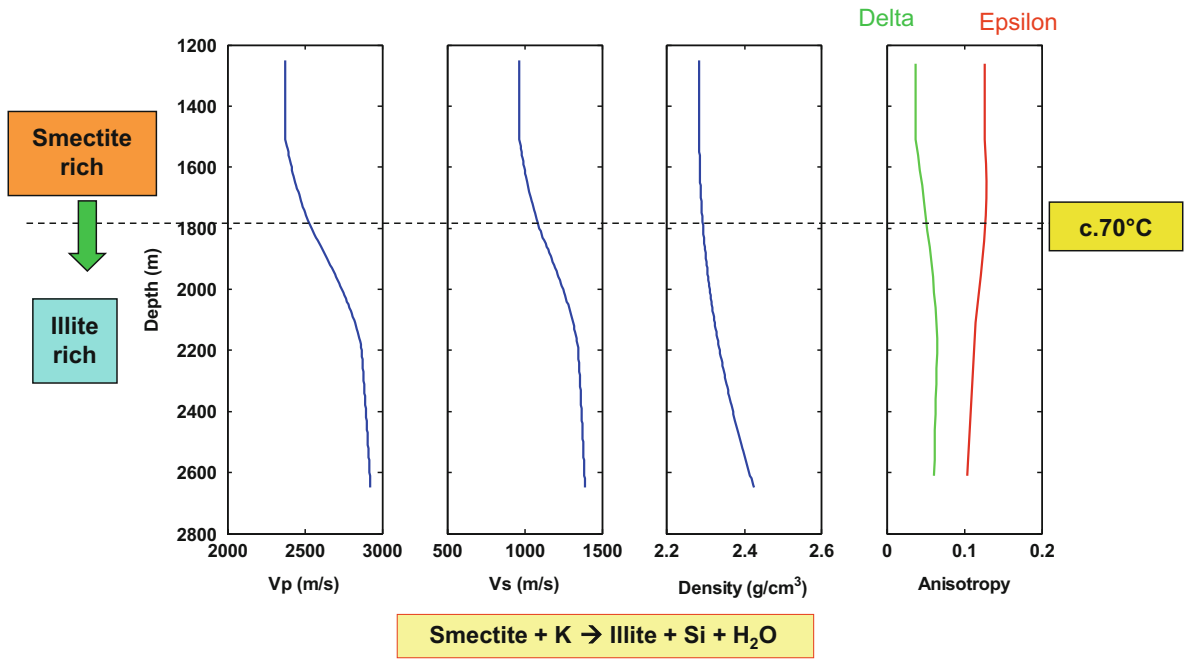

Fig. 18.16 Modelled rock physics depth trends of shales, showing the effect of illitisation of marine smectite-rich shales. (From Avseth et al. 2008)

the velocities for sands increase drastically as we go from the unconsolidated regime with only mechanical compaction to the cemented regime with predominantly chemical compaction. The onset of quartz cement happens at about 70°C corresponding to about 2 km burial depth, in accordance with the observations made in Fig. 18.8, and as documented from thin-section analysis (Fig. 18.9).

We apply the Shale Compaction Model (Dræge et al. 2006, Ruud et al. 2003) to estimate the anisotropic effective properties in mechanically compacted shales. The first seismically important mineral reaction in shales is commonly the smectite to illite reaction. This reaction has several implications for the shale; the soft smectite is replaced by stiffer illite, which might be distributed differently in the rock, the reaction produces water, the volume of solids is decreased (i.e. illite has a denser mineral structure than smectite), quartz is generated as a by-product, and porosity is reduced by chemical compaction. Where the shales lie within the chemical compaction regime, a new set of rock physics models is applied to estimate the seismic properties. The anisotropic version of a Differential Effective Medium (DEM) model and Self Consistent Approximation (SCA) are used to approximate the elongated pores and grains in shales (Hornby et al. 1994). In the present discussion, pores in chemically compacted shales are considered to be isolated, while the pores in the mechanical compaction regime are connected (cf. Dræge et al. 2006). We define a transition zone, where the properties change from the mechanical to chemical regime. In Fig. 18.16, the initial shale (<1,500 m) is considered to be smectite-rich, while the deeper (>2,200 m) illite-rich shale is somewhat stiffer. There are two counteracting effects on anisotropy. The initial alignment of grains leads to pores becoming more aligned and hence increasing anisotropy. But decreasing porosity leads to decreasing anisotropy, culminating in the anisotropic properties of the solid material at zero porosity. The pores introduce higher anisotropy than the solid, since pores commonly are weaker orthogonal to the longest axis, while the solids are less dependent on direction of wave propagation. In addition to *Vp*, *Vs* and density, we estimate the Thomsen parameters of anisotropy, δ and ε, which can be significant during interpretation of angle-dependent seismic reflectivity (AVO analysis), see Sect. 18.8.

18.6 Seismic Fluid Sensitivity and Gassmann Theory for Fluid Substitution

Seismic fluid sensitivity is determined by a combination of porosity and pore-space stiffness. A softer rock will have a larger sensitivity to fluids than a stiffer rock at the same porosity. The most common theory for fluid substitution is the so-called Gassmann theory (Gassmann 1951, Mavko et al. 2009, Avseth et al. 2005), which describes the fluid sensitivity of porous, isotropic rocks at seismic frequency (i.e. when no grain-scale viscous flow effects will stiffen the rock frame). The Gassmann theory is very important in all rock physics modelling, therefore both the formulation and workflow of the theory are included in this overview chapter.

For the fluid substitution problem there are two fluid effects that must be considered: the change in rock bulk density, and the change in rock compressibility. The compressibility of a dry rock (reciprocal of the rock bulk modulus) can be expressed quite generally as the sum of the mineral compressibility and an extra compressibility due to the pore space:

$$\frac{1}{K_{dry}} = \frac{1}{K_{mineral}} + \frac{\phi}{K_{\phi}} \tag{18.11}$$

where ϕ is the porosity, K_{dry} is the dry rock bulk modulus, $K_{mineral}$ is the mineral bulk modulus, and K_{ϕ} is the pore space stiffness defined by:

$$\frac{1}{K_{\phi}} = \frac{1}{v_{pore}} \frac{\partial v_{pore}}{\partial \sigma} \tag{18.12}$$

Here, v_{pore} is the pore volume, and σ is the increment of hydrostatic confining stress from the passing wave. Poorly consolidated rocks, rocks with microcracks, and rocks at low effective pressure, are generally soft and compressible and have a small K_{ϕ}. Stiff rocks that are well cemented, lacking microcracks, or at high effective pressure have a large K_{ϕ}. In terms of the popular, but idealised, ellipsoidal crack models, low aspect ratio cracks have small K_{ϕ} and rounder large aspect ratio pores have large K_{ϕ}.

Similarly, the compressibility of a saturated rock can be expressed as:

$$\frac{1}{K_{sat}} = \frac{1}{K_{mineral}} + \frac{\phi}{K_{\phi} + \frac{K_{fluid}K_{mineral}}{K_{fluid}+K_{mineral}}} \tag{18.13}$$

or approximately as:

$$\frac{1}{K_{sat}} \approx \frac{1}{K_{mineral}} + \frac{\phi}{K_{\phi} + K_{fluid}} \tag{18.14}$$

where K_{fluid} is the pore fluid bulk modulus. Comparing Eqs. (18.11) and (18.14), we see that changing the pore fluid will modify the effective pore space stiffness (Avseth et al. 2005). From Eq. (18.14) we see also the well-known result that a stiff rock, with large pore space stiffness K_{ϕ}, will have a small sensitivity to fluids, and a soft rock, with small K_{ϕ}, will have a large sensitivity to fluids.

Equations (18.11) and (18.13) together are equivalent to Gassmann's (1951) relations. We can algebraically eliminate K_{ϕ} from Eqs. (18.11) and (18.13) and write Gassmann's relations in one of the more familiar, but less intuitive, forms:

$$\frac{K_{sat}}{K_{mineral} - K_{sat}} = \frac{K_{dry}}{K_{mineral} - K_{dry}} + \frac{K_{fluid}}{\phi\left(K_{mineral} - K_{fluid}\right)} \tag{18.15}$$

and the companion result for the shear modulus

$$\mu_{sat} = \mu_{dry} \tag{18.16}$$

Gassmann's equations (18.15) and (18.16) predict that for an isotropic rock, the rock bulk modulus will change if the fluid changes, but the rock shear modulus will not.

These dry and saturated moduli, in turn, are related to P-wave velocity $V_P = \sqrt{(K + (4/3)\mu)/\rho}$ and S-wave velocity $V_S = \sqrt{\mu/\rho}$, where ρ is the bulk density given by

$$\rho = \phi\rho_{fluid} + (1 - \phi)\rho_{mineral} \tag{18.17}$$

In the equations above, ϕ is normally interpreted as the total porosity, though in shaly sands the better choice is to use effective porosity during fluid substitution (Dvorkin et al. 2007). Another uncertainty stems from Gassmann's assumption that the rock is monomineralic. Clay-rich sandstones actually violate the

monomineralic assumption, but an effective mineral modulus can be approximated via the Hill's average or Hashin-Shtrikman modelling (see Mavko et al. 2009). Another issue is whether the clay should be considered only as part of the mineral frame, or should the bound water that constitutes part of the clay mineral be considered part of the fluid when we do Gassmann fluid substitution? If the latter, then the functional Gassmann porosity is actually larger than the total porosity, but the pore fluid should be considered a muddy suspension containing clay particles.

Gassmann's relations were originally derived to describe the change in rock modulus from one pure saturation to another – from dry to fully brine-saturated, from fully brine-saturated to fully oil-saturated, etc. Domenico (1976) suggested that mixed gas-oil-brine saturations can also be modelled with Gassmann's relations, if the mixture of phases is replaced with an effective fluid with bulk modulus $\overline{K}_{fluid}$ and density $\overline{\rho}_{fluid}$ given by

$$\frac{1}{\overline{K}_{fluid}} = \frac{S_{gas}}{K_{gas}} + \frac{S_{oil}}{K_{oil}} + \frac{S_{br}}{K_{br}} = \left\langle \frac{1}{K_{fluid}(x,y,z)} \right\rangle \tag{18.18}$$

$$\overline{\rho}_{fluid} = S_{gas}\rho_{gas} + S_{oil}\rho_{oil} + S_{br}\rho_{br} = \left\langle \rho_{fluid}(x,y,z) \right\rangle \tag{18.19}$$

where $S_{gas,oil,br}$,$K_{gas,oil,br}$, and $\rho_{gas,oil,br}$ are the saturations, bulk moduli, and densities of the gas, oil, and brine phases. The operator $\langle \cdot \rangle$ refers to a volume average and allows for more compact expressions, where $K_{fluid}(x, y, z)$ and $\rho_{fluid}(x, y, z)$ are the spatially varying pore fluid modulus and density.

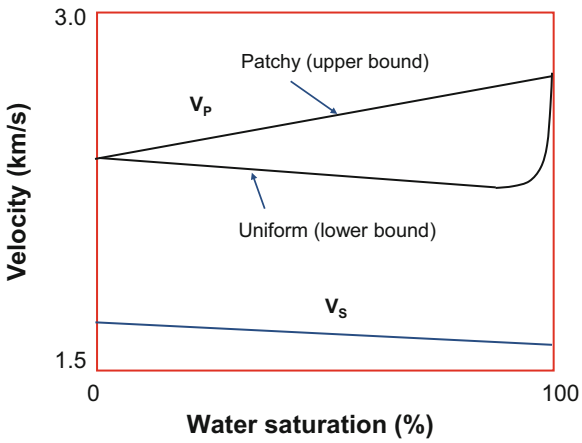

Fig. 18.17 Uniform versus patchy saturation, mixing gas and water in a porous rock according to Gassmann theory

Substituting Eq. (18.18) into Gassmann's relation is the procedure most widely used today to model fluid effects on seismic velocity and impedance for low frequency field applications. The fluid properties are obtained through the Batzle and Wang (1992) equations, and these normally comprise brine salinity, gas gravity, oil reference density, gas/oil ratio (GOR), temperature and pore pressure.

A problem with mixed fluid phases is that velocities depend not only on saturations but also on the spatial distributions of the phases within the rock (Fig. 18.17). Equation (18.18) is applicable only if the gas, oil, and brine phases are mixed uniformly at a very small scale, so that the different wave-induced increments of pore pressure in each phase have time to diffuse and equilibrate during a seismic period (Mavko et al. 2009). Equation (18.18) is the Reuss (1929) average or "isostress" average, and it yields an appropriate equivalent fluid when all pore phases have the same wave-induced pore pressure. A simple dimensional analysis suggests that during a seismic period pore pressures can equilibrate over spatial scales smaller than $L_c \approx \sqrt{\kappa K_{fluid}/f\eta}$, where f is the seismic frequency, κ is the permeability, and η and K_{fluid} are the viscosity and bulk modulus of the most viscous fluid phase. We refer to this state of fine-scale, uniformly mixed fluids as "uniform saturation."

In contrast, saturations that are heterogeneous over scales larger than ~L_c will have wave-induced pore pressure gradients that cannot equilibrate during the seismic period, and Eq. (18.18) will fail. We refer to this state as "patchy saturation". Patchy saturation, or "fingering" of pore fluids, can easily be caused by spatial variations in wettability, permeability or shaliness. The rock modulus with patchy saturation can be approximated by Gassmann's relation, with the mixture of phases replaced by the "isostrain" (Voigt 1910) average effective fluid (Mavko et al. 2009):

$$\overline{K}_{fluid} = S_{gas}K_{gas} + S_{oil}K_{oil} + S_{br}K_{br}. \tag{18.20}$$

This implies that patchy saturation will cause higher velocities and impedances than when the same fluids are mixed at a fine scale. The fact that the fluids cannot move freely and equilibrate during a

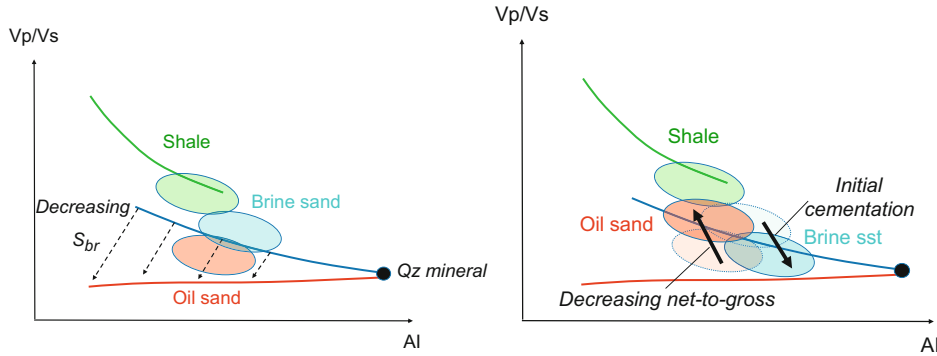

Fig. 18.18 Rock physics templates (RPTs) can be made from the rock physics models in Fig. 18.6 combined with Gassmann theory, to define regions where expected facies and fluids will plot. In particular, the *Vp/Vs* ratio is known to be a great fluid discriminator in siliciclastic environments. Homogeneous, unconsolidated sands filled with oil are normally well separated from ditto brine-filled sands in an RPT of *Vp/Vs* versus acoustic impedance (*AI*), c.f. schematic illustration in the upper crossplot. However, the effect of initial cement will reduce the fluid sensitivity of sandstones and the *Vp/Vs* ratio of cemented brine sandstones can be similar to the *Vp/Vs* ratio of unconsolidated sands filled with oil. The effect of net-to-gross will normally move data in the opposite direction in a *AI-Vp/Vs* crossplot. Hence, oil sands with relatively low net-to-gross can have higher *Vp/Vs* ratio than homogeneous brine sands with initial cement, c.f. schematic illustration in lower crossplot. (Adapted from Avseth et al. 2009)

seismic wave period results in a stiffer effective rock than is the case with uniform saturation where the fluids have time to equilibrate.

Equation (18.20) appears to be an upper bound, and data seldom fall on it, except at very low gas saturations.

18.7 Rock Physics Templates

We can combine the depositional and diagenetic trend models presented above with Gassmann fluid substitution, and make charts or templates of rock physics models for predicting lithology and presence of hydrocarbons. We refer to these locally constrained charts as *Rock Physics Templates* (RPTs), a methodology first presented by Ødegaard and Avseth (2004). Furthermore, we expand on the rock physics diagnostics presented earlier as we create RPTs of seismic parameters, in our case acoustic impedance ($AI = V_P \cdot \rho$) versus *Vp/Vs* ratio (Fig. 18.18). This will allow us to perform rock physics analysis not only of well log data, but also of seismic data (e.g. elastic inversion results).

The motivation behind RPTs is to generate an atlas or collection of relevant rock physics models for different basins and areas. Then, the ideal interpretation workflow becomes a fairly simple two-step procedure: (1) Select the appropriate RPT for the area and depth under investigation, using well log data to verify the validity of the selected RPT(s). (2) Use the selected and verified RPT(s) to interpret elastic inversion results. RPT interpretation of well log data may also be an important stand-alone exercise both for the interpretation and quality control of well log data, and in order to assess seismic detectability of different fluid and lithology scenarios.

The RPTs are site (basin) specific and are constrained by local geological factors, including lithology, mineralogy, burial depth, diagenesis, pressure and temperature. All these factors must be considered when generating RPTs for a given basin. In particular, it is essential to include only the expected lithologies for the area under investigation when generating the rock physics templates. The water depth and the burial depth determine the effective pressure, pore pressure and lithostatic pressure. The pore pressure is important for the calculation of fluid properties, and for determining the effective stress on the grain contacts of the rock frame carrying the overburden.

In modelling RPTs we also need to know the acoustic properties of mud-filtrate, formation water and hydrocarbons in the area of investigation. Required input parameters include temperature, pressure, brine salinity, gas gravity, oil reference density and GOR. In areas where hydrocarbons have yet to be encountered, gas gravity can be assumed (normally 0.6–0.8).

However, oil reference density is more uncertain. Also, the seismic response of oil can be difficult to distinguish from that of brine. One should, however, expect oil to show values similar to low gas saturation in *AI* versus *Vp/Vs* ratio crossplots. Regarding saturation distribution, we have assumed uniform distribution in the template modelling (Ødegaard and Avseth 2004), which gives the famous effect where residual amounts of gas will produce almost the same seismic properties as commercial amounts of gas. However, a patchy distribution of gas would have shown a more linear change in seismic properties with increasing gas saturation (cf. Fig. 18.17).

Pore fluid sensitivity in reservoir sandstones is highly affected by reservoir heterogeneity and sandstone microstructure, and it is therefore important to include these geological factors in the rock physics analysis. As already indicated, initial cement reduces the pressure and fluid sensitivity of the sandstones. Figure 18.18 shows schematically the outline of a rock physics template, where calibrated rock physics models have been selected that fit local data observations (well log data or seismic inversion data) of various lithologies and pore fluids. The presence of diagenetic quartz cement will move brine-saturated sandstone data in an *AI* versus *Vp/Vs* crossplot to an area of very low *Vp/Vs*, where we would expect hydrocarbon-saturated sandstones to plot. By contrast, reservoir heterogeneity and decreasing net-to-gross associated with interbedded sands and shales tend to move data points in the direction of the shale cluster. The cement effect is a microstructural effect, whereas the net-to-gross is related to the scale of shale/sand interbedding and is frequency dependent. In the case where the interbedded shale is relatively soft compared to the sand, the net-to-gross effect will counteract the effect of cement on effective rock stiffness, hence these two effects will have opposite trends in the *AI*-*Vp/Vs* crossplot. The schematic, but qualitatively correct illustration in Fig. 18.18 demonstrates why it is important to include these geological factors when analysing the rock physics properties and seismic fluid sensitivity in reservoir sandstones.

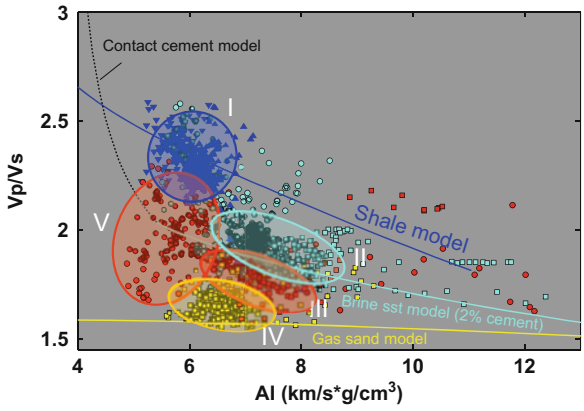

Fig. 18.19 RPT of *Vp/Vs* versus acoustic impedance (*AI*) for target zone (Palaeocene) of two North Sea wells. Cluster I is the cap rock shale in both wells, II comprises the brine sandstones in both wells, III and IV are reservoir sandstones in well 1 filled with oil and gas, respectively. V is the upper oil zone in well 2, with *Vp/Vs* higher than the brine sandstones, and *AI* lower than the gas sandstones in well 1. This is counter-intuitive, and must be explained by difference in sandstone quality, c.f. Fig. 18.18. (Adapted from Avseth et al. 2009)

Figure 18.19 shows an RPT including data from two neighbouring wells penetrating Palaeocene sands in the North Sea (Avseth et al. 2009). One well penetrated a thick, turbiditic gas sand with a thin oil-leg, whereas the adjacent well penetrated a turbidite sand filled with oil. Furthermore, one of the wells is the same one as was used in the rock physics diagnostics in Figs. 18.7 and 18.8, and in the depth trend modelling above (Fig. 18.15). It turns out that the sandstone quality changes from one well to the other, and this drastically distorts the fluid sensitivity to hydrocarbons. The gas-saturated Heimdal sands in well 1 show a small increase in acoustic impedance, while the oil-saturated sands in well 2 show a significant drop in acoustic impedance. This drastic change in sandstone quality over a short distance will also yield a corresponding change in seismic signatures, see next section below.

18.8 Seismic Reservoir Characterisation Using AVO

About 30 years ago, William Ostrander, published a ground-breaking paper on offset-dependent reflectivity (Ostrander 1984). He showed that gas-saturated sands capped by shales would cause an **a**mplitude **v**ariation with **o**ffset (AVO effect) in pre-stack seismic data (Fig. 18.20). Shortly after, AVO technology became a commercial tool for the oil industry, quickly gaining in popularity as it was now possible to explain seismic amplitudes in terms of rock properties. The technique proved successful for hydrocarbon

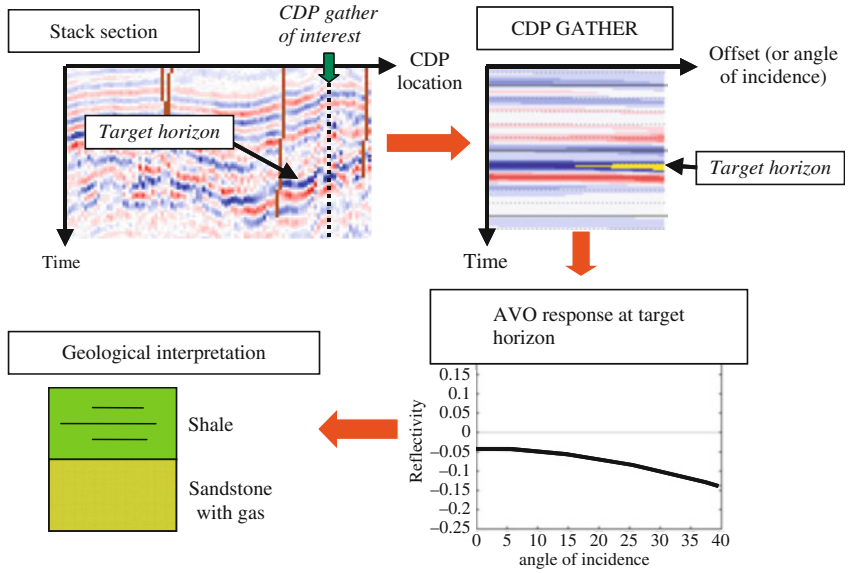

Fig. 18.20 Schematic illustration of the principles in AVO analysis. (From Avseth et al. 2005)

prediction in many areas of the world, yet in some cases it failed. The technique suffered from ambiguities caused by lithological effects, tuning effects and overburden effects. It turned out that even seismic processing and acquisition effects could cause false AVO anomalies. Application of AVO analysis was therefore reduced. However, in many of these cases it was incorrect use of the technique that was responsible for the failure, not the technique itself. In the last decade we have observed a revival of the AVO technique. This is due to the improvement of 3D seismic technology, better pre-processing routines, more frequent shear-wave logging that can better constrain AVO modelling, improved understanding of rock physics properties, greater data capacity, more focus on cross-disciplinary aspects of AVO and, last but not least, more awareness among the users of the potential pitfalls.

The technique provides the seismic interpreter with information about pore fluids and lithologies, which complements the conventional interpretation of seismic facies, stratigraphy and geomorphology. The reflection coefficient for plane elastic waves as a function of reflection angle at a single interface, also referred to as the AVO response, is described by the complicated Zoeppritz equations (Zoeppritz 1919). For analysis of P-wave reflections, a well-known approximation is given by Aki and Richards (1980), assuming weak layer contrasts:

$$R(\theta_1) \approx \frac{1}{2}\left(1 - 4p^2V_s^2\right)\frac{\Delta\rho}{\rho} + \frac{1}{2\cos^2\theta}\frac{\Delta V_p}{V_p} - 4p^2V_S^2\frac{\Delta V_S}{V_S}, \tag{18.21}$$

where:

$$p = \frac{\sin\theta_1}{V_{P1}} \quad \theta = (\theta_1 + \theta_2)/2 \approx \theta_1$$

$$\Delta\rho = \rho_2 - \rho_1 \quad \rho = (\rho_2 + \rho_1)/2$$

$$\Delta V_P = V_{P2} - V_{P1} \quad V_P = (V_{P2} + V_{P1})/2$$

$$\Delta V_S = V_{S2} - V_{S1} \quad V_S = (V_{S2} + V_{S1})/2$$

In the formulae above, p is the ray parameter, θ_1 is the angle of incidence, and θ_2 is the transmission angle. V_{P1} and V_{P2} are the P-wave velocities above and below a given interface, respectively. Similarly, V_{S1} and V_{S2} are the S-wave velocities, while ρ_1 and ρ_2 are densities above and below this interface.

The approximation given by Aki and Richards can be further approximated (Shuey 1985):

$$R(\theta) \approx R(0) + G \cdot \sin^2\theta + F\left(\tan^2\theta - \sin^2\theta\right), \quad (18.22)$$

where

$$R(0) = \frac{1}{2}\left(\frac{\Delta V_P}{V_P} + \frac{\Delta\rho}{\rho}\right),$$

$$G = \frac{1}{2}\frac{\Delta V_P}{V_P} - 2\frac{V_S^2}{V_P^2}\left(\frac{\Delta\rho}{\rho} + 2\frac{\Delta V_S}{V_S}\right)$$

$$= R(0) - \frac{\Delta\rho}{\rho}\left(\frac{1}{2} + \frac{2{V_S}^2}{{V_P}^2}\right) - \frac{4{V_S}^2}{{V_P}^2}\frac{\Delta V_S}{V_S},$$

and

$$F = \frac{1}{2}\frac{\Delta V_P}{V_P}.$$

This form can be interpreted in terms of different angular ranges, where $R(0)$ is the normal incidence reflection coefficient, G describes the variation at intermediate offsets and is often referred to as the AVO gradient, whereas F dominates the far offsets, near critical angle. Normally, the range of angles available for AVO analysis is less than 30°–40°. Therefore, we only need to consider the two first terms, valid for angles less than 30° (Shuey 1985):

$$R(\theta) \approx R(0) + G \cdot \sin^2\theta \quad (18.23)$$

Transverse isotropy in the cap-rock shale can affect the AVO gradient significantly. During feasibility studies of AVO, it is important to investigate this effect. The P-wave reflectivity in case of transverse isotropy in the cap-rock can be expressed as the sum of the isotropic reflectivity and the anisotropic reflectivity (Kim et al. 1993):

$$R_{PP}(\theta) = R_{IPP}(\theta) + R_{APP}(\theta) \quad (18.24)$$

where the isotropic term is the same as Eq. (18.21) or its approximations (Eqs. 18.22 or 18.23), and the anisotropic term is given by:

$$R_{APP}(\theta) = -0.5\delta_1 \cdot \sin^2(\theta) - 0.5\varepsilon_1 \cdot \sin^2(\theta) \cdot \tan^2(\theta). \quad (18.25)$$

As we see from this expression, one of the Thomsen parameters, δ, is affecting the same offset range as the contrast in *Vp/Vs* ratio (i.e. the AVO gradient), whereas ε is affecting larger offsets. Often during AVO analysis, anisotropy is ignored, in particular in shallow sediments where poorly compacted shales are assumed to be isotropic. As we showed in Fig. 18.16, the Tertiary shales in the North Sea have some anisotropy, which was also demonstrated by Golikov et al. (2013), and we will later show a sensitivity study of the effect of anisotropy on the AVO signatures of a North Sea Tertiary oil and gas field. Golikov et al. (2013) also demonstrated the effect of anisotropy on elastic parameters and associated AVO signatures due to interbedding of sands and shales within a reservoir.

The most common and practical way to do AVO analysis of seismic data is to make crossplots of the zero-offset reflectivity ($R(0)$) versus the AVO gradient (G), assuming isotropic reservoir and cap-rock. These attributes are estimated from pre-stack seismic gathers using simple least-square regressions, according to Eq. (18.23). Often it is assumed that calibrated near stack seismic data, where the near offset traces have been stacked together, is representative of the zero offset reflectivity. Furthermore, it can be assumed that the difference between the far stack seismic (where the far offset traces have been stacked together) and the near stack seismic is a scaled version of the AVO gradient. Hence, AVO crossplots can be made directly from near and far stack seismic sections. Brine-saturated sands interbedded with shales, situated within a limited depth range and at a particular locality, normally follow a well defined "background trend" in AVO crossplots. A common and recommended approach in qualitative AVO crossplot analysis is to recognise the "background" trend and then look for data points that deviate from this trend. Deviations from the background trend in an AVO crossplot may be indicative of hydrocarbons.

Rutherford and Williams (1989) suggested a classification scheme of AVO responses for different types of gas sands (Fig. 18.21). They defined three AVO classes based on where the top of the gas sands will locate in an $R(0)$ versus G crossplot. The crossplot is split up into four quadrants. In a crossplot with $R(0)$ along x-axis and G along y-axis, the 1st quadrant is where $R(0)$ and G are both positive values (upper right quadrant). The 2nd is where $R(0)$ is negative and G is positive (upper left quadrant). The 3rd is where both $R(0)$ and G are negative (lower left quadrant). Finally,

the 4th quadrant is where $R(0)$ is positive and G is negative (lower right quadrant). The AVO classes must not be confused with the quadrant numbers. Class I plots in the 4th quadrant with positive $R(0)$ and negative gradients. These represent hard events with relatively high impedance and low Vp/Vs ratio compared to the cap-rock. Class II represents sands with weak intercept, but strong negative gradient. These can be hard to see on the seismic, because they often yield dim-spots on stacked sections. Class III is the AVO category that is normally associated with bright spots. These plot in the 3rd quadrant in $R(0)$-G crossplots, and are associated with soft sands saturated with hydrocarbons.

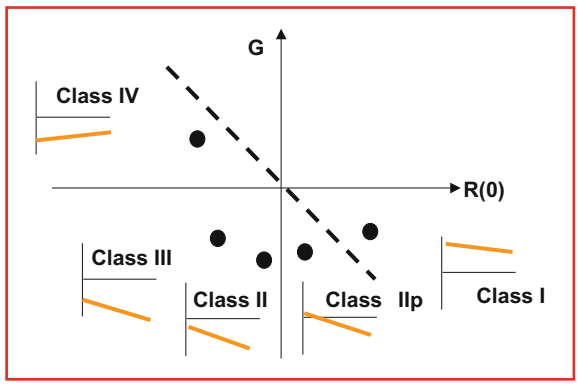

Fig. 18.21 Rutherford and Williams AVO classes, originally defined for gas sands (class I, II and III), along with the added classes IV (Castagna and Swan 1997) and IIp (Ross and Kinman 1995). Figure is adapted from Castagna and Swan (1997)

Ross and Kinman (1995) separated between a class IIp and class II anomaly. Class IIp has a weak, but positive intercept and a negative gradient, causing a polarity change with offset. This class will disappear on full stack sections. Class II has a weak, but negative intercept and negative gradient, hence no polarity change. This class may be observed as a negative amplitude on a full offset stack.

Castagna and Swan (1997) extended the classification scheme of Rutherford and Williams to include a 4th class, plotting in the 2nd quadrant. These are relatively rare, but occur when soft sands with gas are capped by relatively stiff cap-rock shales characterized by Vp/Vs ratios slightly higher than in the sands (i.e. very compacted or silty shales).

Figure 18.22 shows a seismic line with two wells indicated as black lines (same wells that are analysed

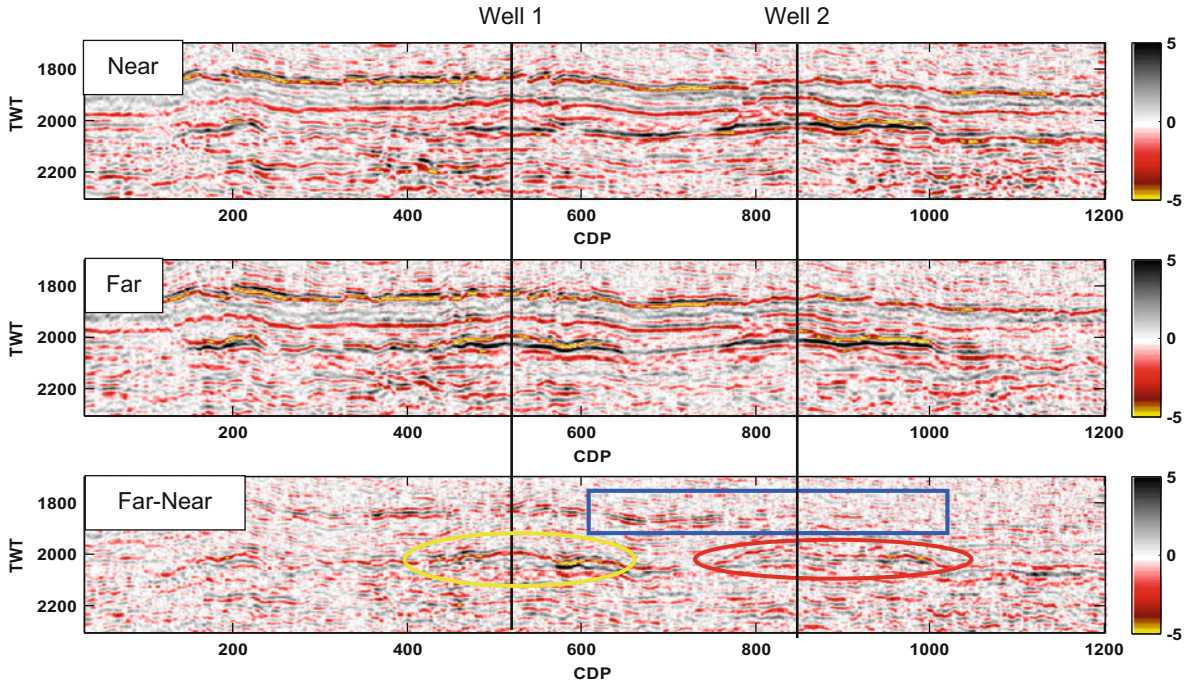

Fig. 18.22 Seismic sections intersecting two wells (same wells that are analysed in Fig. 18.19), including near stack, far stack, and the estimated far-near stack. The *blue square* indicates the window where a background trend is defined. The *yellow ellipse* highlights the gradient anomaly of the gas and oil discovery of Well 1. The *red ellipse* highlights an adjacent oil discovery of Well 2. (Adapted from Avseth et al. 2009)

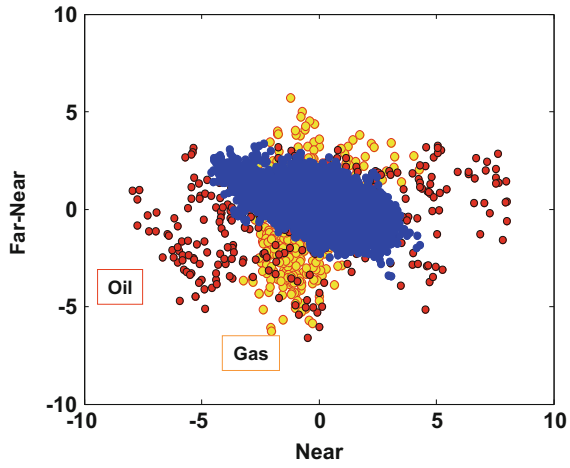

Fig. 18.23 Intercept (Near) versus gradient (i.e. Far-Near) for the seismic stack section in Fig. 18.22. Only data from the selected polygons are included. The *blue points* represent the background trend right above the target, the *yellow points* represent data from the gas (and oil) discovery in Well 1 in Fig. 18.22, whereas the *red data points* represent data from the oil discovery in Well 2 in Fig. 18.22. (Adapted from Avseth et al. 2009)

in Fig. 18.19). One well penetrated a thick, turbiditic gas sand with a thin oil-leg, whereas the adjacent well penetrated a turbidite sand filled with oil. However, it turned out that the AVO anomaly of the oil sand is stronger than for the gas discovery (Fig. 18.23), and the oil sands show a negative bright near stack response and a class III AVO anomaly, whereas the gas sands show a dim (i.e. close to zero) near stack response and a class II AVO anomaly. These observations are counter-intuitive if the reservoir sands are similar. Avseth et al. (2009) demonstrated the importance of rock texture, in particular cement volume, as well as net-to-gross, and how these geological factors affected the seismic signatures of hydrocarbons within these sands.

The deviation from the background trend in an AVO crossplot can be quantified in terms of the fluid factor (Smith and Gidlow 1987, Fatti et al. 1994) as follows:

$$\Delta F = \frac{8}{5} R(0) - \kappa[R(0) - G] \tag{18.26}$$

where κ is a constant at a given depth, depending on the background *Vp/Vs* ratio, χ, and the slope of the *Vp-Vs* relationship of the modelled shale trend, m:

$$\kappa = \frac{m}{\chi} \tag{18.27}$$

Commonly, m is selected to be the slope of the '*Mudrock Line*' (Castagna et al. 1985), where $m = 1.16$. Similarly, the background *Vp/Vs* ratio (χ) is often set equal to 2, giving a κ value of 0.58. However, with modelled shale trends, we can estimate more realistic depth-dependent values of κ and get a better control on the expected background trend to be used in the fluid factor (Avseth et al. 2008). Both gas- and oil-filled sands will cause negative fluid factor anomalies relative to the background brine trend. However, chemical compaction has a significant impact on the absolute value of the fluid factor, which is directly related to the fact that the fluid sensitivity decreases with depth and increasing rock stiffness (Fig. 18.24).

An improved understanding of rock physics depth trends in sands and shales helps us to better understand how AVO signatures change with depth. By conducting AVO depth trend modelling, we can verify the feasibility of AVO analysis as a function of burial depth and diagenesis, and thereby extrapolate to other burial depths. This can be a useful task in exploration or appraisal, where we want to extend our search to slightly deeper or shallower prospects adjacent to existing discoveries. This is demonstrated in Fig. 18.25 where we have done AVO two-layer modeling of reservoir sandstone capped by shale at three different depths for the case shown in Fig. 18.15. (1) at 1,600 m where only mechanical compaction is occurring; (2) at 2,000 m in a transition zone where initial chemical compaction has taken place; and (3) at 2,400 m where the sandstones are moderately to well cemented. In this reflectivity modelling, we include both isotropic (whole lines) and anisotropic (dashed lines) AVO modelling. In the latter case we assume the cap rock shale to be transversely isotropic, with the Thomsen parameters estimated from the shale modelling shown in Fig. 18.16. We perform the modelling for water-, oil- and gas-filled reservoir. We conclude that the effect of anisotropy is minimal in this case, and can be ignored in the further AVO analysis. The effect of burial, on the other hand, is dramatic. Within

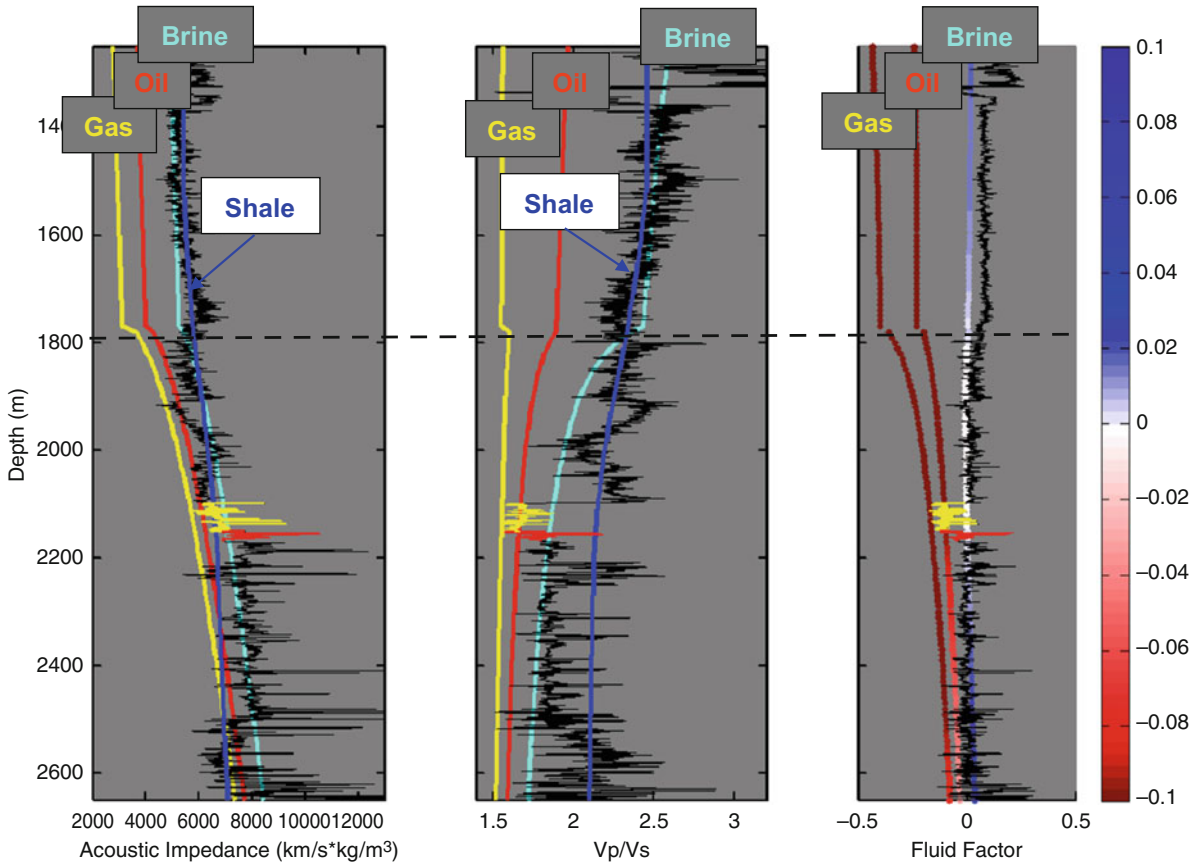

Fig. 18.24 Seismic depth trends and expected fluid factor. Note that both oil and gas sands show large negative fluid factor values down to about 2,300–2,400 m burial depth, whereas brine sands show weak or positive fluid factor values for all depth ranges. Gas sands seem to give negative fluid factor even deeper than the modelled window, beyond 2,600 m. The gas and oil zone in the well log data also show a relatively strong fluid factor anomaly, as expected from the depth trends. (Adapted from Avseth et al. 2008)

a few hundred metres, the AVO signatures change significantly, due to compaction. The oil response can be quite similar to either a slightly deeper gas response or a slightly shallower water response. In general, we go from a class IV to III AVO regime for hydrocarbons at the shallowest level, to a class II to III in the middle level, and finally to a class I to II at the deeper level, following the AVO classification system of Rutherford and Williams (1989), see Fig. 18.21. This shows how important it is to honour burial history and compaction during AVO analysis.

We can now estimate the fluid factor attribute for the seismic line shown in Fig. 18.22. The fluid factor can be derived from near- and far-stack amplitudes using the formula:

$$\Delta F = Near - \eta \cdot (Far - Near) \tag{18.28}$$

Here, η is not the same as κ in the earlier formulation of the fluid factor, since *Far-Near* is not exactly the same as the AVO gradient. However, the two-term AVO makes a linear relationship between the *Far-Near* and the AVO gradient, and therefore η and κ can also be easily correlated. Assuming the far stack to be around 30° and the near stack to be at 0° (normally the far stack will be representative for slightly lower angles than 30°, whereas near stack will be

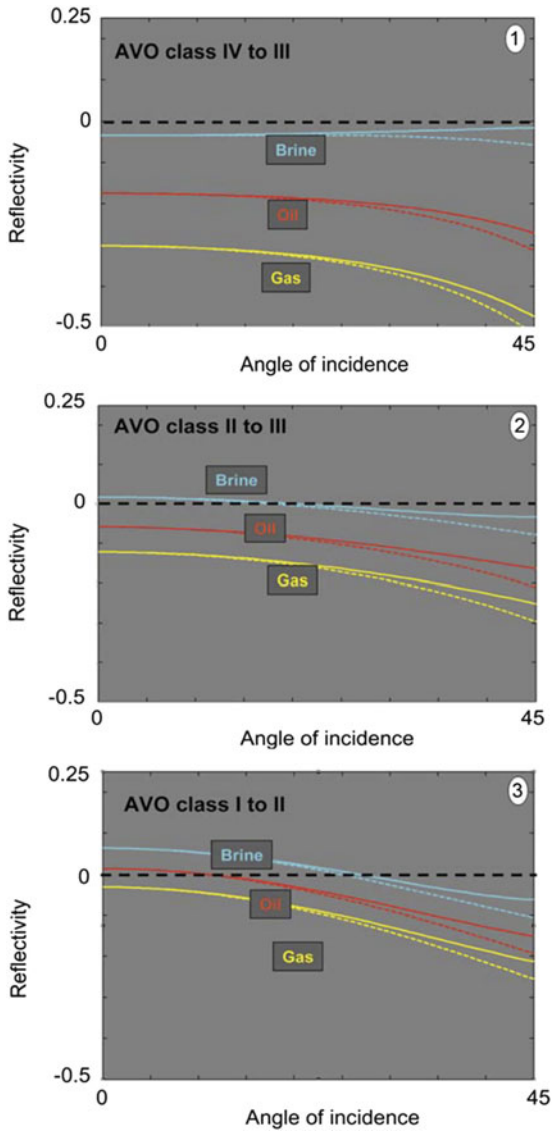

Fig. 18.25 P-to-P-wave AVO reflectivity modelling at three different depth levels, with reference to Figs. 18.15 and 18.16: (1) At 1,600 m burial depth we obtain AVO class IV for brine sands and class III for hydrocarbons. Note that the anisotropy effect (*dashed lines*) is actually changing the sign of the gradient for brine sands from slightly positive to slightly negative. (2) At 2,000 m burial depth, we observe a weaker fluid sensitivity, and the brine sands have almost zero near-stack response, but there are significant negative gradients for all fluid scenarios. (3) At 2,400 m burial depth, the brine sandstones show a class I AVO signature, whereas oil- and gas-filled sandstones show a more class II AVO response. For all cases, the anisotropy starts becoming significant beyond about 30° angle of incidence, and should not impact our 2-term AVO analysis for this case

representative for angles slightly higher than 0°) we obtain the following approximate relationship between the gradient and the *Far-Near*:

$$\begin{aligned} Far - Near &= R(30) - R(0) \\ &= G \cdot \sin^2(30) = G \cdot 0.25 \end{aligned} \tag{18.29}$$

Solving for the background trend, that is when $\Delta F = 0$, we obtain:

$$Near = \frac{-20\kappa}{8 - 5\kappa}(Far - Near) \tag{18.30}$$

and hence:

$$\eta = \frac{-20\kappa}{8 - 5\kappa} \tag{18.31}$$

The slope of the background trend in the *Near* versus *Far-Near* stack is $1/\eta$, and this shows that we can in fact estimate the expected background trend for uncalibrated (but offset balanced) range limited stacks using the modelled shale trends as illustrated above (Fig. 18.16). This can be a useful task to verify the correct amplitude balancing between near- and far-stack data during AVO crossplot analysis.

Based on the shale model trends, we estimate the value of η to be of the order 2.5. This means the background trend of the shale in the AVO crossplot is relatively flat, equaling -0.4, i.e., $Far\text{-}Near = -0.4Near$. We observe indeed that the shale background trend is relatively flat (blue cloud in Fig. 18.23). Using this background trend, the resulting fluid factor attribute in Fig. 18.26 shows that both the gas and the oil discoveries stand out as strong fluid factor anomalies, whereas the background data is relatively weak.

We also estimate the difference between intercept and gradient, which has been shown to be close to $\Delta Vs/Vs$ (Fatti et al. 1994, Avseth et al. 2005). This attribute should not be significantly affected by pore fluids, but very sensitive to lithology and cementation. Figure 18.26 shows the fluid factor crossplot and line superimposed with the $\Delta Vs/Vs$ attribute for the seismic line intersecting both well 1 and well 2. As expected, both the gas and the oil discoveries show strong fluid factors, whereas only well 1 (gas discovery) shows a strong change in $\Delta Vs/Vs$ at the top of the reservoir. This tallies with the observations from the well log

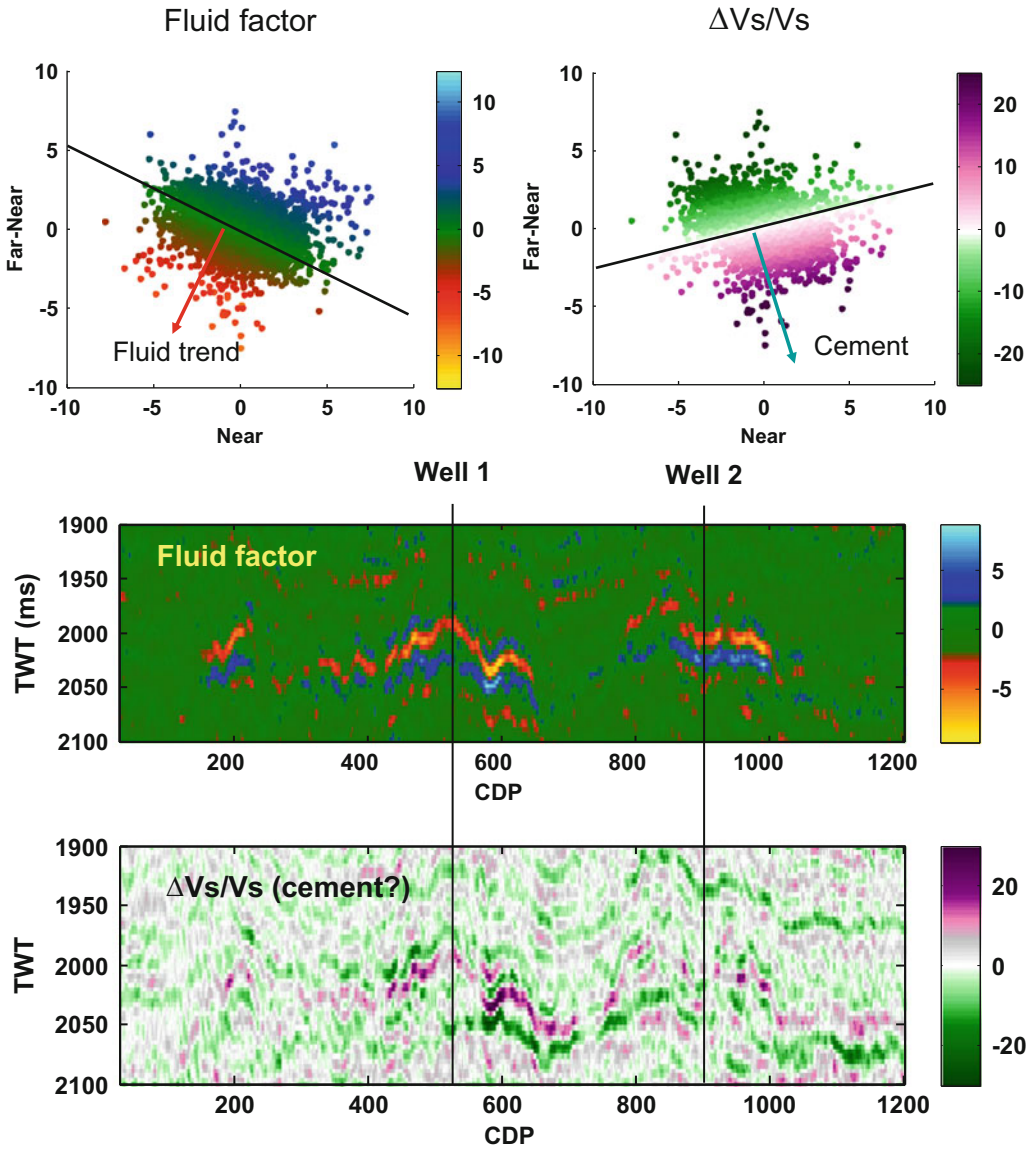

Fig. 18.26 AVO crossplots with fluid factor and ditto with *ΔVs/Vs* as coloured attribute, for the seismic section intersecting the two wells in Fig. 18.22. The fluid factor attribute represents the deviation from the local background shale trend. The *ΔVs/Vs* attribute reflects rock stiffness, and is expected to be an appropriate attribute to detect initial quartz cement in the Heimdal Formation sandstones. The resulting AVO attributes (*lower*) show strong fluid factor values at both well locations, whereas the *ΔVs/Vs* attribute shows a much stronger contrast at well 1 than at well 2. Avseth et al. (2009) documented that the *uppermost part* of Heimdal sandstones in well 2 are less cemented than the Heimdal sandstones in well 1 (cf. RPT observations in Fig. 18.19), and this can also explain the different AVO responses at the two well locations

data, and also with the rock physics estimation of relatively low cement volume at the top of the Heimdal sands in well 2 (see Avseth et al. 2009). It further explains why we have such drastically different AVO signatures in the two wells, while the counter-intuitive AVO anomalies for oil and gas are explained by the local change in rock texture. With two seismic parameters ($R(0)$ and G) it is possible to discriminate the fluid effects from the lithological effects.

A problem when interpreting AVO crossplots is that a given point in the crossplot does not correspond to a unique combination of rock properties. Many

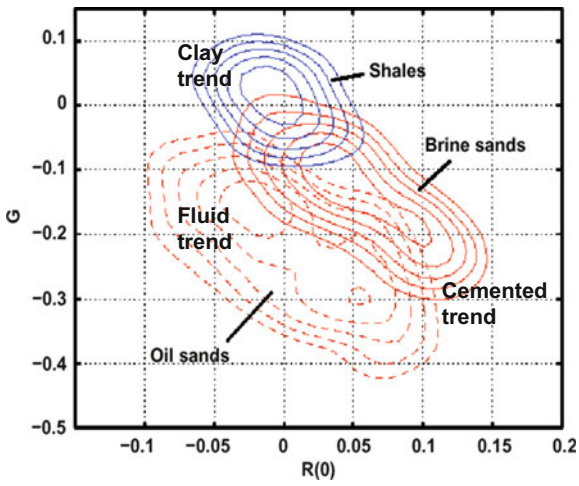

Fig. 18.27 AVO contour plots or probability density functions (pdfs) for main facies and fluids in the Glitne field. Only the iso-probability contours of 50% and larger are included for each group. The $R(0)$ and G pdfs nicely separate the three facies groups, but there are significant overlaps. (Adapted from Avseth et al. 2001a)

combinations of rock properties will yield the same $R(0)$ and G. Moreover, due to natural variability in geological and fluid parameters, one given geological scenario may span a relatively large possible outcome area in the AVO crossplot, not just a discrete point. Hence, a hydrocarbon-like AVO response might occasionally result from a brine-associated reflection, and hydrocarbon-saturated sands might not always produce an anomalous AVO response; this problem was seen in the RPT crossplots in Fig. 18.18. One way to resolve this uncertainty is to create probability crossplots of various categories of lithology and pore fluid scenarios. These can be based on statistical analysis of well log data and/or rock physics models (Avseth 2000, Avseth et al. 2001a, b; Mukerji et al. 2001). Each category is plotted as a "contour map", almost like topographical maps (Fig. 18.27). Here, the "mountain tops" represent the most likely location of a given class. It is very important to be aware that the contours of different facies and fluids are overlapping each other. This implies that an observed set of $R(0)$ and G can represent more than one category. This is

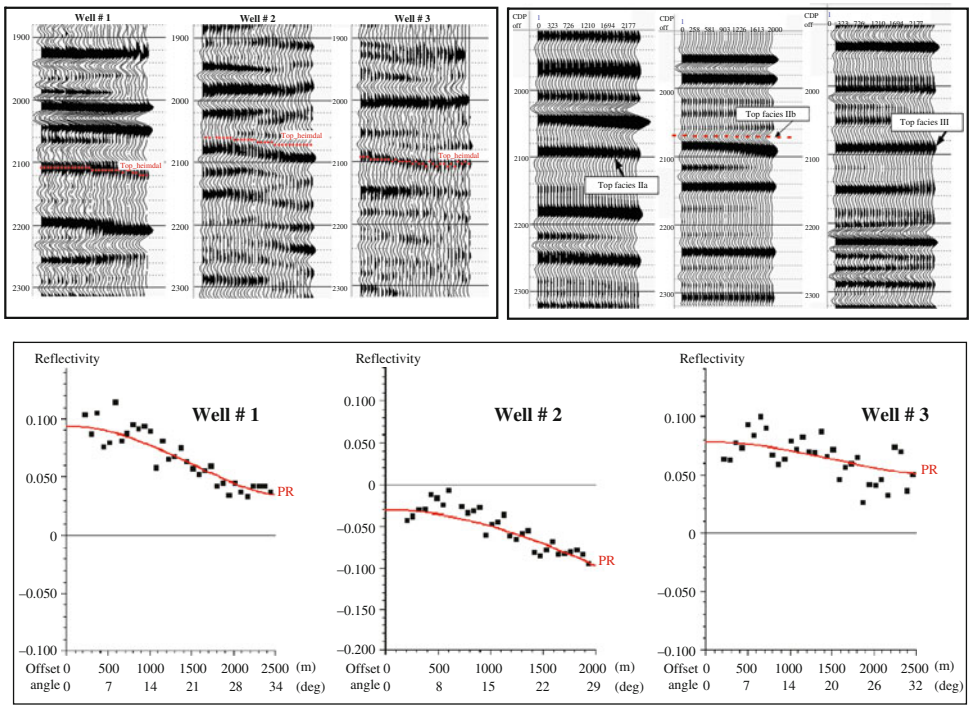

Fig. 18.28 Real CDP gathers (*upper left*), synthetic CDP gathers (*upper right*), and AVO curves (*lower*) for three wells penetrating the Glitne turbidite system (Fig. 18.1) at different locations. Note the drastic change in AVO signature from the feeder-channel (cemented sandstone filled with brine), to the lobe-channel (unconsolidated sand filled with oil), and to the lobe margin (interbedded sand-shale and shaly sandstone). (Adapted from Avseth et al. 2001a)

one reason why AVO analysis, used alone, can give misleading results. In addition, these crossplots are often affected by noise in the seismic data. Nevertheless, as we see in Fig. 18.27, we often observe that we need both intercept ($R(0)$) and gradient (G) in order to separate facies and fluid types from seismic data. Or put another way, we often need to do AVO to discriminate lithology from fluids on seismic data.

Avseth et al. (2001a) applied the contour plots in Fig. 18.27 to conduct an AVO analysis and predict seismic lithofacies and pore fluids from the pre-stack seismic amplitudes in the Glitne Field which are depicted in the amplitude map in Fig. 18.1. As demonstrated in Fig. 18.1, the depositional trends in the Glitne turbidite system do affect the seismic amplitudes. This is also confirmed by deterministic AVO analysis of CDP gathers (see Fig. 18.28) at the three well locations depicted in Fig. 18.1. The dramatic variability in the lateral facies distribution, going from a relatively proximal feeder-channel environment to a relatively distal lobe and lobe margin environment, has great impact on the seismic signatures in this turbidite system.

The next step is facies and pore fluid prediction from 3D seismic data. 3D AVO inversion is performed on the turbidite system using Hampson-Russell's AVO software. Again, we focus only on the horizon representing the top of the system (Top Heimdal). Figure 18.29 shows the three dimensional topography (in two-way traveltime) of this seismic horizon, where the geometries of the feeder-channel and the lobe

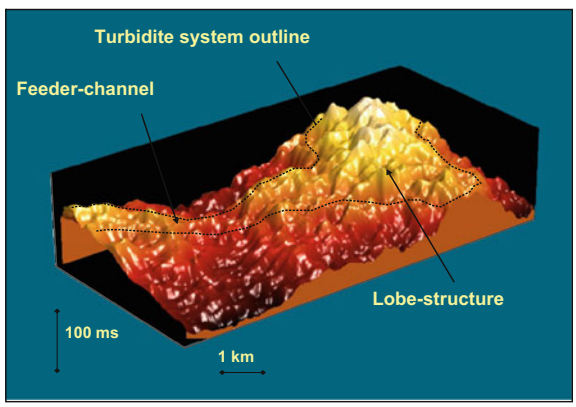

Fig. 18.29 Three-dimensional seismic topography of Top Heimdal horizon (two-way travel time). The depositional geometry of a feeder-channel and fan lobe is outlined (compare to Fig. 18.1). (Adapted from Avseth et al. 2001a)

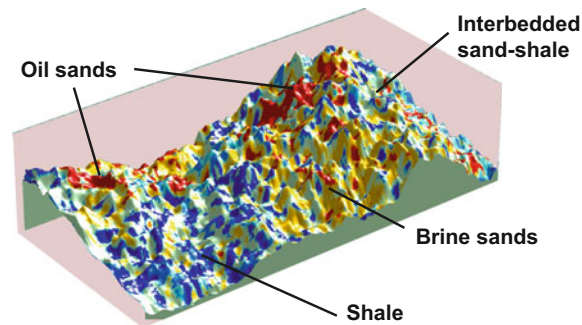

Fig. 18.31 Lithofacies prediction beneath Top Heimdal seismic horizon, in the Glitne Field. Note the prediction of most likely oil sands in the top lobe structure, as well as in the *upper part* of the feeder channel. The latter is not realistic, knowing that a well is penetrating brine-filled feeder-channel sands *right* outside the amplitude map. However, as we see in the AVO contour plots in Fig. 18.27, we expect some ambiguity and overlap between brine sands and oil sands. (Adapted from Avseth et al. 2001a)

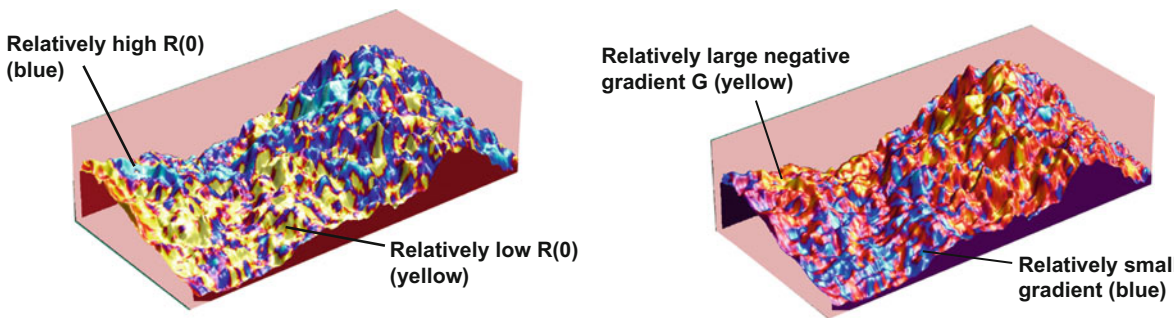

Fig. 18.30 Intercept (R(0)) and AVO gradient (G) estimated along Top Heimdal horizon in the Glitne Field. (Adapted from Avseth et al. 2001a)

structure are outlined. The inversion gives us $R(0)$ and G over the whole area across this horizon slice. Figure 18.30 shows the intercept $R(0)$ and the gradient G. These plots allow us to predict the most likely seismic lithofacies underlying this horizon. This is done by combining the $R(0)$ and G inverted from the seismic with the $R(0)$–G contour plots, also referred to as probability density functions (pdfs), which are derived from well log data. Before we can do this, however, the inverted parameters must be calibrated to the well log values (see Avseth et al. 2005 for further details).

We apply the Mahalanobis distance method to calculate the most likely facies group and pore fluid from the seismic data (Avseth et al. 2005). The results are shown in Fig. 18.31. We predict oil-saturated sands in the lobe area where the lobe is structurally highest. The rest of the lobe area is most likely water-saturated according to the prediction. Furthermore, we predict oil-filled sands in the upper feeder-channel. Outside the submarine fan, the most likely facies is predicted to be dominated by shale. The sands are mainly predicted in the channel and lobe areas while oil is predicted in the structurally highest areas of the sand deposits. The depositional patterns predicted from the AVO analysis agree well with the expected facies associations in the Glitne submarine fan. This case example demonstrates that AVO and quantitative seismic interpretation can be particularly useful in geological settings where facies prediction is not easily obtained from conventional seismic interpretation.

Finally, a case example from the Barents Sea will be shown, where rock physics properties and associated AVO signatures may change rapidly and in a complex manner due to extensive tectonic uplift episodes. Avseth et al. (2003) introduced a methodology to constrain AVO classification by rock physics depth trends. However, they only considered unconsolidated sediments in continuously subsiding basins. Taking

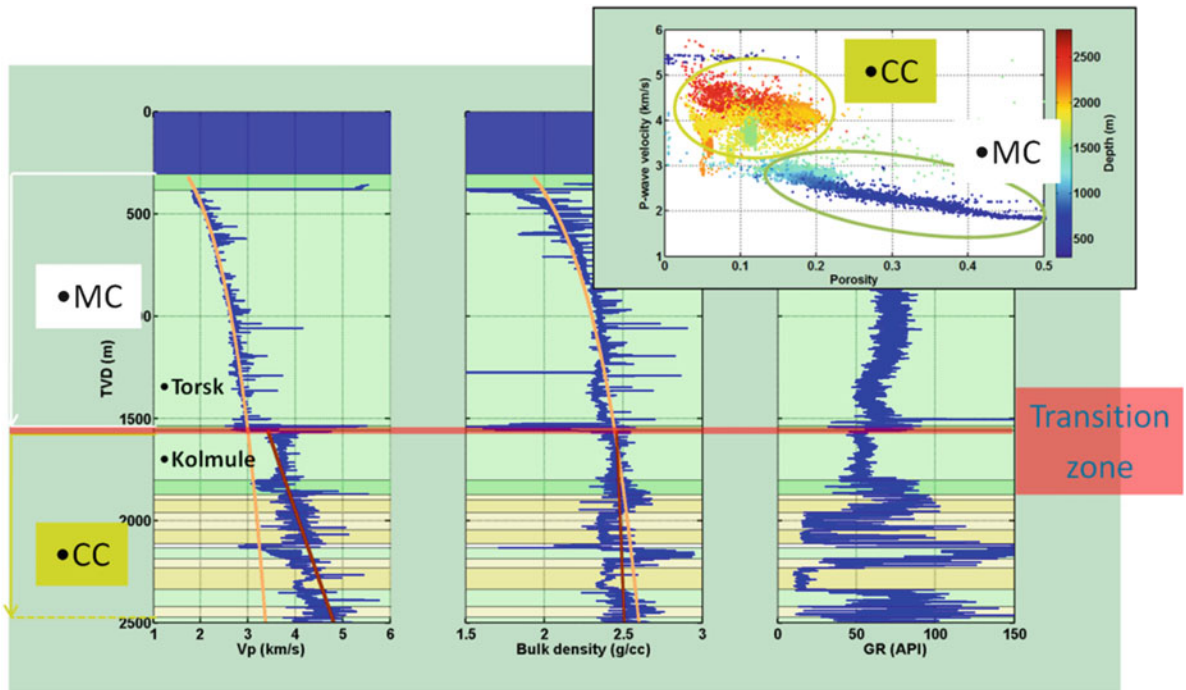

Fig. 18.32 Well log data (including *Vp*, density and gamma ray) from well 7201/2-1 (Myrsildre), which was a well with oil shows in the Kolmule Fm. Note the velocity and density depth trends. However, there is a big jump in velocity as we go from Torsk Fm to Kolmule Fm; this corresponds to a change in diagenesis going from mechanical compaction domain to chemical compaction domain, i.e. transition from sediments to rocks. The corresponding change in a porosity-velocity crossplot is shown in the upper right corner, showing the elastic stiffening effect of chemical compaction (CC) of rocks compared to mechanically compacted (MC) sediments. (Adapted from Lehocki et al. 2012)

into account diagenesis and tectonic events, we can predict compaction trends and associated seismic velocities in areas with more complex burial history involving both mechanical and chemical compaction, as well as uplift episodes and corresponding erosion. The resulting rock physics trends help us to better constrain AVO inversion and classification under such circumstances.

Lehocki et al. (2012) proposed a methodology for statistical classification of fluids and facies in areas with tectonic uplift based on rock physics depth trends, and they demonstrated the methodology on seismic AVO data from the Loppa High area in the Barents Sea, where there has been significant tectonic uplift. The main objective of that study was to perform seismic reservoir prediction and hunt for Upper Cretaceous Kolmule Formation sands with good reservoir quality in a structural setting near the Loppa High. Furthermore, the goal was to do both pre- and post-drill predictions of a prospect. A neighbouring well (Fig. 18.32) was used for local calibration. This well is located down-flank of the structural high of interest, and Kolmule Formation sands are not encountered in it. Note, however, the sudden jump in velocity as we go from Torsk Formation shales to Kolmule Formation shales. The gamma ray log and density log show only small changes at this interface. Regional work has indicated that this is the transition from the mechanical to chemical compaction domain, and is in agreement with observations made by Storvoll et al. (2005) and Thyberg et al. (2009).

Rock physics models are compared and calibrated to the observed velocities, for both domains. The Hertz-Mindlin contact theory is used for the loose sediments above the onset of cement, whereas the Dvorkin-Nur contact cement model was utilised to model the velocities of sandstones in the chemical compaction domain. The rock physics models are furthermore adjusted in depth until we obtain an optimal match between observed sonic well log data and modelled velocities. A maximum burial depth of c. 2,500 m is estimated, implying that the net uplift is around 1,300 m. We therefore expect the reservoirs to have been buried at temperatures high enough to initiate chemical compaction.

AVO data, including intercept and gradient, were extracted from a window around the seismic horizon representing the Top Kolmule sst (Fig. 18.33). Based on the rock physics burial trends, we created AVO pdfs for different lithofacies and fluids representative for the target burial depth (Fig. 18.34). This was done both pre- and post-drill of the prospect, with slightly different calibrations. The AVO pdfs were then used to classify the calibrated AVO data. The resulting maps of lithofacies and fluids are shown in Fig. 18.35. The prospect was drilled and the presence of gas in the

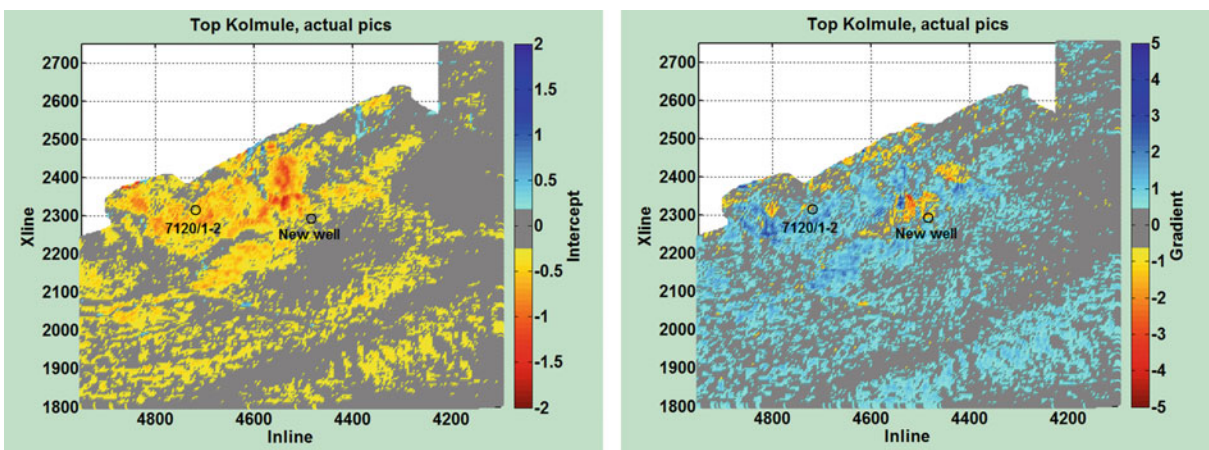

Fig. 18.33 AVO data from the Loppa High near the Skalle prospect. Intercept (*left*) and gradient (*right*). Note the negative intercept and gradients around the prospect well location. (Adapted from Lehocki et al. 2012)

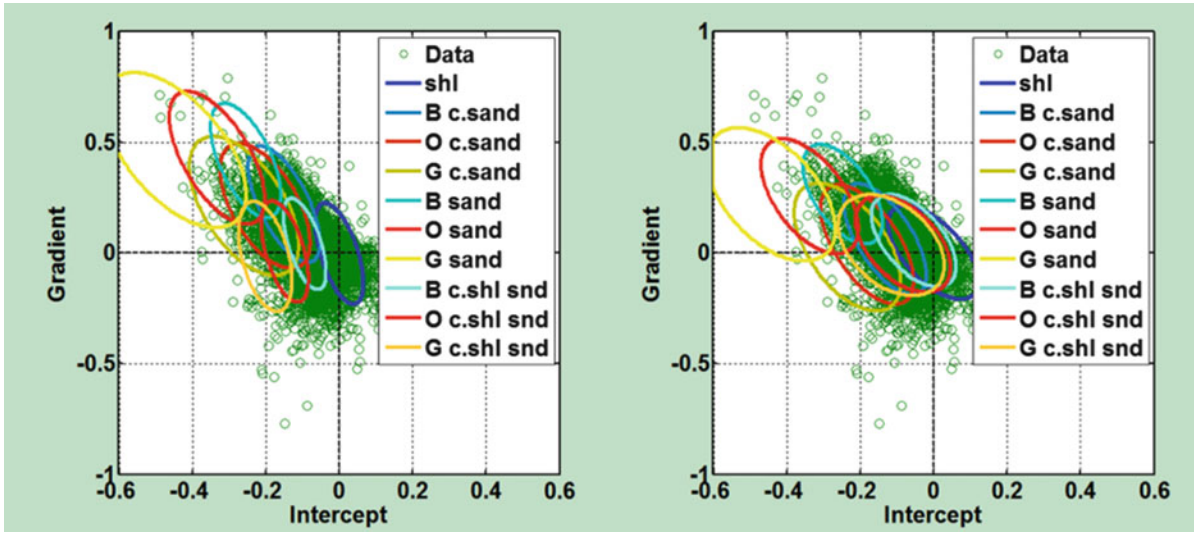

Fig. 18.34 Calibrated intercept and gradient with juxtaposed isoprobability contours ($P>0.5$) of different facies and fluids, including cemented sandstones (c.sand), cemented shaly sandstones (c.shl.snd), loose sands (sand), and shales (shl); with brine (B), oil (O) or gas (G) in the sandy facies. The calibration done prior to the prospect well, is shown to the *left*; the calibration done after the prospect well was drilled is shown to the *right*. Note the slight rotation of the data and the location of the isoprobability ellipses. (Adapted from Lehocki et al. 2012)

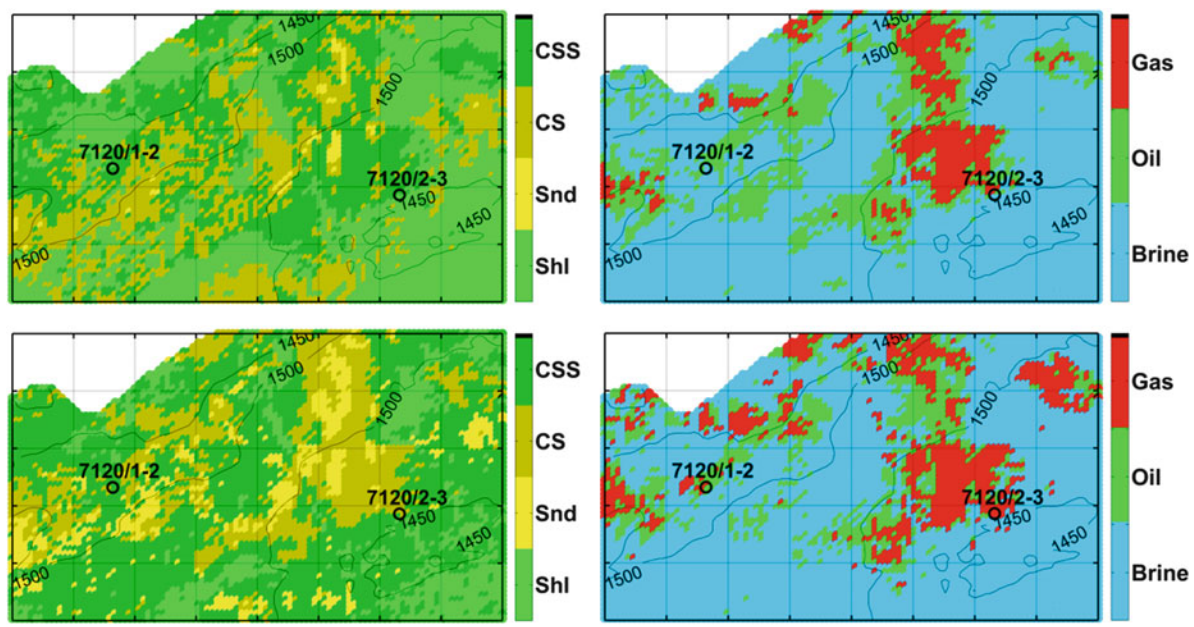

Fig. 18.35 AVO classification results; Lithofacies (*CSS* Cemented shaly sandstones, *CS* Cemented sandstone, *Snd* Loose sand, *Shl* Shale) to the *left* and pore fluids to the *right*. Pre-drill of 7120/2-3 in the *upper two subplots*, and post-drill of this well in the *lower two subplots*. Note that the fluid distributions are very similar, indicating that the calibration and classification based on well 7120/1-2 is giving quite good results. We predict somewhat less shales, and some more of the loose sands, with information from the new well. The well 7120/1-2 had oil shows, whereas well 7120/2-3 encountered a gas-filled heterolithic Kolmule sandstone, as predicted both pre- and post-drill. (Adapted from Lehocki et al. 2012)

Kolmule sandstone was confirmed for the prospect. The workflow was repeated post-drill to obtain an even better calibration of the rock physics depth trends, and the results are also shown in Fig. 18.35; as we see the differences are quite small, demonstrating the benefit of the AVO information calibrated by a nearby well, prior to drilling this prospect.

18.9 Conclusions

In this chapter we have demonstrated how we can apply rock physics tools to relate geological parameters and trends to seismic properties, and thereby predict rock and fluid characteristics from seismic amplitude data. The focus of this chapter has been to present a workflow for quantitative seismic interpretation during petroleum exploration. Rock physics ultimately serves as a toolbox for lithology and fluid substitution, where we can understand local well log observations and extrapolate to certain expected "what if" scenarios, either in terms of depositional or compactional trends, or in terms of changes in pore fluids. The models can also be applied to predict or classify reservoir parameters from sonic and seismic data. We have demonstrated our cross-disciplinary approach on well log and seismic data from selected areas on the Norwegian shelf where reservoir sands are prone to change drastically both because of facies variability, diagenetic alterations and tectonic impact. We have also demonstrated the importance of understanding the rock physics and seismic properties of shales during seismic reservoir prediction using AVO analysis.

Acknowledgements Thanks to Prof. Gary Mavko and Prof. Tapan Mukerji at Stanford University for collaboration over a long period and contributions to the work presented here. Thanks to Arild Jørstad and Hans Oddvar Augedal at Lundin-Norway for geological input to the Palaeocene sands studied in this chapter; also thanks to Aart-Jan van Wijngaarden, Erik Ødegaard, Torbjørn Fristad, and Anders Dræge at Statoil for fruitful discussions and input to the work included in this chapter. I also acknowledge Prof. Ran Bachrach at Tel Aviv University, and Prof. Tor Arne Johannesen at University of Bergen, for valuable discussions. Finally, I would like to thank Ivan Lehocki at Lehocki Geospace and Håvard Buran at Lundin-Norway for contributions to the AVO case study in the Barents Sea, and to Tor Veggeland at Tullow Oil Norge for valuable input on the Glitne case study presented here.

Further Reading

Aki, K. and Richards, P.G. 1980. Quantitative Seismology: Theory and Methods. San Francisco: W.H. Freeman, 948 pp.

Anselmetti, F. and Eberli, G.P. 1997. Sonic velocity in carbonate sediments and rocks. In: Palaz, I. and Marfurt, K.J. (eds.), Carbonate Seismology. Society of Exploration Geophysicists, Houston, TX, pp. 53–73.

Avseth, P. 2000. Combining rock physics and sedimentology for seismic reservoir characterization of North Sea turbidite systems. Ph.D. thesis, Stanford University, 200 pp.

Avseth, P., Dræge, A., van Wijngaarden, A.-J., Johansen, T.A. and Jørstad, A. 2008. Shale rock physics and implications for AVO analysis: A North Sea demonstration. The Leading Edge 27, 788–797.

Avseth, P., Dvorkin, J., Mavko, G. and Rykkje, J. 2000. Rock physics diagnostic of North Sea sands: Link between microstructure and seismic properties. Geophysical Research Letters 27, 2761–2764.

Avseth, P., Flesche, H. and van Wijngaarden, A.-J. 2003. AVO classification of lithology and pore fluids constrained by rock physics depth trends. The Leading Edge 22(10), 1004–1011.

Avseth, P., Johansen, T.A., Bakhorji, A. and Mustafa, H.M. 2014. Rock physics modeling guided by depositional and burial history in low-to-intermediate-porosity sandstones. Geophysics 79, D115–D122.

Avseth, P., Jørstad, A., van Wijngaarden, A.-J. and Mavko, G. 2009. Rock physics estimation of cement volume, sorting and net-to-gross in North Sea sandstones. The Leading Edge 28, 98–108.

Avseth, P., Mukerji, T., Jørstad, T., Mavko, G. and Veggeland, T. 2001a. Seismic reservoir mapping from 3-D AVO in a North Sea turbidite system. Geophysics 66, 1157–1176.

Avseth, P., Mukerji, T. and Mavko, G. 2005. Quantitative Seismic Interpretation – Applying Rock Physics Tools to Reduce Interpretation Risk. Cambridge University Press, Cambridge, 376 pp.

Avseth, P., Mukerji, T., Mavko, G. and Dvorkin, J. 2010. Rock physics diagnostics of depositional texture, diagenetic alterations and reservoir heterogeneity in high porosity siliciclastic sediments and rocks - A review of selected models and suggested workflows. Geophysics 75, A31–A47.

Avseth, P., Mukerji, T., Mavko, G. and Tyssekvam, J.A. 2001b. Rock physics and AVO analysis for lithofacies and pore fluid prediction in a North Sea oil field. The Leading Edge 20, 429.

Batzle, M. and Wang, Z. 1992. Seismic properties of pore fluids. Geophysics 57, 1396–1408.

Bjørlykke, K. 1998. Clay mineral diagenesis in sedimentary basins – A key to the prediction of rock properties; Examples from the North Sea Basin. Clay Minerals 33, 15–34.

Bjørlykke, K. and Egeberg, P.K. 1993. Quartz cementation in sedimentary basins. AAPG Bulletin 77, 1538–1548.

Box, G.E.P. and Draper, N.R. 1987. Empirical Model Building and Response Surfaces. New York, NY: John Wiley and Sons, 669 pp.

Brevik, I., Ahmadi, G.R., Hatteland, T. and Rojas, M.A. 2007. Documentation and quantification of velocity anisotropy in shales using wireline log measurements. The Leading Edge 26(3), 272–277.

Castagna, J.P., Batzle, M.L. and Eastwood, R.O. 1985. Relationships between compressional-wave and shear-wave velocities in clastic silicate rocks. Geophysics 50, 571–581.

Castagna, J.P. and Swan, H.W. 1997. Principles of AVO crossplotting. The Leading Edge 16, 337–342.

Domenico, S.N. 1976. Effect of brine-gas mixture on velocity in an unconsolidated sand reservoir. Geophysics 41, 882–894.

Dræge, A. 2009. Constrained rock physics modeling. The Leading Edge 28, 76–80.

Dræge, A., Jakobsen, M. and Johansen, T.A. 2006. Rock physics modeling of shale diagenesis. Petroleum Geoscience 12(1), 49–57.

Dvorkin, J. and Gutierrez, M. 2002. Grain sorting, porosity and elasticity. Petrophysics 43, 185–196.

Dvorkin, J., Mavko, G. and Gurevich, B. 2007. Fluid substitution in shaley sediment using effective porosity. Geophysics 72, O1–O8.

Dvorkin, J. and Nur, A. 1996. Elasticity of high-porosity sandstones: Theory for two North Sea datasets. Geophysics 61, 1363–1370.

Fatti, J.L., Smith, G.C., Vail, P.J., Strauss, P.J. and Levitt, P.R. 1994. Detection of gas in sandstone reservoirs using AVO analysis: A 3-D seismic case history using the Geostack technique. Geophysics 59, 1362–1376.

Gassmann, F. 1951. Uber die elastizitat poroser medien. Vier der Natur Gesellschaft 96, 1–23.

Giles, M.R., Indrelid, S.L., Beynon, G.V. and Amthor, J. 2000. The origin of large-scale quartz cementation: Evidence from large data sets and coupled heat-fluid mass transport modeling. In: Worden, R.H. and Morad, S (eds.), Quartz Cementation in Sandstones. International Association of Sedimentologists Special Publication 29, Blackwell, Oxford, pp. 21–38.

Golikov, P., Avseth, P., Stovas, A. and Bachrach, R. 2013. Rock physics interpretation of heterogeneous and anisotropic turbidite reservoirs. Geophysical Prospecting 61, 448–457.

Hamilton, E.L. 1956. Low sound velocities in high porosity sediments. Journal of the Acoustical Society of America 28, 16–19.

Han, D. 1986. Effects of porosity and clay content on acoustic properties of sandstones and unconsolidated sediments. Unpublished Ph.D. dissertation, Stanford University.

Hashin, Z. and Shtrikman, S. 1963. A variational approach to the elastic behavior of multiphase materials. Journal of the Mechanics and Physics of Solids 11, 127–140.

Hornby, B.E., Schwartz, L.M. and Hudson, J.A. 1994. Anisotropic effective-medium modeling of the elastic properties of shales. Geophysics 59, 1570–1583.

Johansen, T.A., Jakobsen, M. and Ruud, B.O. 2002. Estimation of the internal structure and anisotropy of shales from borehole data. Journal of Seismic Exploration 11, 363–381.

Kim, K.Y., Wrolstad, K.H. and Aminzadeh, F. 1993. Effects of transverse isotropy on P-wave AVO for gas sands. Geophysics 58, 883–888.

Lehocki, I.L. and Avseth, P. 2010. Rock physics quantification of diagenetic cement (EAGE Extended Abstract P244). In 72nd EAGE Conference and Exhibition, Barcelona.

Lehocki, I.L., Avseth, P., Buran, H. and Jørstad, A. 2012. Statistical AVO classification in areas with diagenesis and tectonic uplift - case examples from the Barents Sea (EAGE Extended Abstract C007). In 74th EAGE Conference and Exhibition, Copenhagen.

MacQuaker, J.H.S., Taylor, K.G. and Gawthorpe, R.L. 2007. High-resolution facies analysis of mudstones: Implications for paleoenvironment and sequence stratigraphic interpretations of offshore ancient mud-dominated successions. Journal of Sedimentary Research 77, 324–339.

Marcussen, Ø., Thyberg, B.I., Peltonen, C., Jahren, J., Bjørlykke, K. and Faleide, J.I. 2009. Physical properties of Cenozoic mudstones from the northern North Sea: Impact of clay mineralogy on compaction trends. AAPG Bulletin 93, 127–150.

Marion, D. 1990. Acoustical, mechanical and transport properties of sediments and granular materials. Ph.D. thesis, Stanford University.

Mavko, G., Mukerji, T. and Dvorkin, J. 2009. The Rock Physics Handbook. Cambridge: Cambridge University Press, 511 pp.

Middleton, G.V. 1973. Johannes Walther's law of the correlation of facies. Geological Society of America Bulletin 84, 979–988.

Mindlin, R.D. 1949. Compliance of elastic bodies in contact. Journal of Applied Mechanics 16, 259–268.

Mondol, N.H., Bjørlykke, K., Jahren, J. and Høeg, K. 2007. Experimental mechanical compaction of clay mineral aggregates – Changes in physical properties of mudstones during burial. Marine and Petroleum Geology 24(5), 289–311.

Mukerji, T., Jørstad, A., Avseth, P., Mavko, G. and Granli, J.R. 2001. Mapping lithofacies and pore-fluid probabilities in a North Sea reservoir: Seismic inversions and statistical rock physics. Geophysics 66(4), 988–1001.

Ødegaard, E. and Avseth, P. 2004. Well log and seismic data analysis using rock physics templates. First Break 22, 37–43.

Ostrander, W.J. 1984. Plane-wave reflection coefficients for gas sands at non-normal angles of incidence. Geophysics 49, 1637–1648.

Peltonen, C., Marcussen, Ø., Bjørlykke, K. and Jahren, J. 2008. Clay mineral diagenesis and quartz cementation in mudstones: The effects of smectite to illite transformation on rock properties. Marine and Petroleum Geology 26(6), 887–898.

Raiga-Clemenceau, J., Martin, J.P. and Nicoletis, S. 1988. The concept of acoustic formation factor for more accurate porosity determination from sonic transit time data. Log Analyst 219, 54–60.

Ramm, M. and Bjørlykke, K. 1994. Porosity/depth trends in reservoir sandstones: assessing the quantitative effects of varying pore-pressure, temperature history and mineralogy, Norwegian Shelf data. Clay Minerals 29, 475–490.

Raymer, L.L., Hunt, E.R. and Gardner, J.S. 1980 (July). An improved sonic transit time-to-porosity transform. Paper presented in 21st Annual Logging Symposium. Society of Professional Well Log Analysis (SPWLA), Lafayette, Louisiana.

Reading, H.G. and Richards, M. 1994. Turbidite systems in deep-water basin margins classified by grain-size and feeder system. AAPG Bulletin 78, 792–822.

Reuss, A. 1929. Berechnung der fliessgrenzen von mischkristallen. Zeitschrift fur Angewandte Mathematik und Mechanik 9, 49–58.

Ross, C.P. and Kinman, D.L. 1995. Non-bright spot AVO: Two examples. Geophysics 60, 1398–1408.

Rutherford, S.R. and Williams, R.H. 1989. Amplitude-versus-offset variations in gas sands. Geophysics 54, 680–688.

Ruud, B.O., Jakobsen, M. and Johansen, T.A. 2003. Seismic properties of shales during compaction (SEG Extended Abstract). In SEG Annual Meeting, Dallas, TX. 4 pp.

Sams, M. and Andrea, M. 2001. The effect of clay distribution on the elastic properties of sandstones. Geophysical Prospecting 49, 128–150.

Shuey, R.T. 1985. A simplification of the Zoeppritz equations. Geophysics 50(4), 609–614.

Smith, G.C. and Gidlow, P.M. 1987. Weighted stacking for rock property estimation and detection of gas. Geophysical Prospecting 35, 993–1014.

Storvoll, V., Bjørlykke, K. and Mondol, N.H. 2005. Velocity-depth trends in Mesozoic and Cenozoic sediments from the Norwegian Shelf. AAPG Bulletin 89(3), 359–381.

Thomsen, L. 1986. Weak elastic anisotropy. Geophysics 51, 1954–1966.

Thyberg, B., Jahren, J., Winje, T., Bjørlykke, K. and Faleide, J.I. 2009. From mud to shale: rock stiffening by micro-quartz cementation. First Break 27, 53–59.

Timoshenko, S.P. and Goodier, J.N. 1934. Theory of Elasticity. New York: McGraw-Hill, 416 pp.

Vernik, L. and Nur, A. 1992. Petrophysical classification of siliciclastics for lithology and porosity prediction from seismic velocities. AAPG Bulletin 76, 1295–1309.

Voigt, W. 1910. Lehrbuch der Kristallphysik. Leipzig: Teubner.

Walderhaug, O., Lander, R.H., Bjørkum, P.A., Oelkers, E.H., Bjørlykke, K. and Nadeau, P.H. 2000. Modelling quartz cementation and porosity in reservoir sandstones: examples from the Norwegian continental shelf. In: Worden, R.H. and Morad, S. (eds.), Quartz Cementation in Sandstones. International Association of Sedimentologists Special Publication 29, Blackwell, Oxford, pp. 39–50.

Walker, R. 1978. Deep-water sandstone facies and ancient submarine fans: Models for exploration for stratigraphic traps. AAPG Bulletin 62, 932–966.

Worden, R.H. and Morad, S. 2000. Quartz cementation in oil field sandstones: A review of the key controversies. In: Worden, R.H. and Morad, S. (eds.), Quartz Cementation in Sandstones. International Association of Sedimentologists Special Publication 29, Blackwell, Oxford, pp. 1–20.

Wyllie, M.J., Gregory, A.R. and Gardner, L.W. 1956. Elastic wave velocities in heterogeneous and porous media. Geophysics 21, 41–70.

Xu, S. and White, R.E. 1995. A new velocity model for clay-sand mixtures. Geophysical Prospecting 43, 91–118.

Yin, H. 1992. Acoustic velocity and attenuation of rocks, isotropy intrinsic anisotropy, and stress induced anisotropy. Ph.D. thesis, Stanford University.

Zoeppritz, K. 1919. Erdbebenwellen VIIIB, Ueber Reflexion and Durchgang seismischer Wellen durch Unstetigkeitsflaechen. Goettinger Nachrichten I, 66–84.